KINEMATICS AND DYNAMICS OF THE ELLIPTICAL GALAXY NGC 5266

Sabrina L. Pakzad
Carlsbad, California, U.S.A.

B.S., University of California, Los Angeles, 2002

M.S., University of Virginia, 2005

Submitted in fulfillment of the academic requirements for the degree of
Master of Science in the Disipline of Physics,
School of Chemical and Physical Sciences,
University of KwaZulu-Natal,

Pietermaritzburg, South Africa
December, 2005

Completed at:
University of KwaZulu-Natal,
University of Virginia

Supervisor : Catherine M. Cress

These studies represent original work by the author
and have not otherwise been submitted in any form of degree or
diploma to any University. Where use has been made of the work
of others it is duly acknowledged in the text.

Catherine M. Cress

Sabrina L. Pakzad

Abstract

In studies of triaxial elliptical galaxies, one of the least observationally studied phenomena is figure rotation. Figure rotation has important consequences for the orbital structure and could explain the survival of steep nuclear cusps. For this project, we thus wish to investigate the possibility of measuring the figure rotation of an elliptical galaxy for which the geometry is approximately known using the Tremaine-Weinberg (TW) method. Originally meant for measuring the pattern speed of barred disk galaxies, we test the validity of the method using NGC 5266, a minor-axis dust-lane elliptical. In the process, the galaxy's line-of-sight velocity distribution (LOSVD) is measured along several slit positions. Measurements of the velocity v, velocity dispersion σ, skewness h_3, and kurtosis h_4 are derived using the Fourier Correlation Quotient method and a Gauss-Hermite series. This work represents the most detailed stellar kinematic measurements of NGC 5266 to date and confirm that it is one of the fastest rotating elliptical galaxies known today (Varnas et al. 1987). We find a maximum velocity of about $167\,\mathrm{km\,s^{-1}}$ at both a PA of 274° and 304°. This is compared to a maximum of $212 \pm 7\,\mathrm{km\,s^{-1}}$ at a PA of 287° found elsewhere (Varnas et al. 1987). The TW method yields significantly different values for the pattern speed. These vary between -19 and $22\,\mathrm{km\,s^{-1}arcsec^{-1}}$. The discrepancy between the results casts doubt on the ability to straightforwardly apply the TW method to elliptical systems, but the study provides some insight into how the method may be more successfully implemented in the future.

Acknowledgements

I would like to thank Dr. Catherine Cress for providing me the opportunity to study in South Africa and for supporting me throughout this project. I would also like to thank Dr. Martin Bureau for allowing me to work on his project and for answering my questions over the past two years. Thanks to funding from both the National Research Foundation in South Africa and the Sigma Xi Grant-in-Aid of Research program, my ten-month long study at the University of KwaZulu-Natal, Pietermartizburg, South Africa and a one-week visit to Columbia University, New York, USA, were completely supported. Lastly, I would like to thank my current advisor at the University of Virginia, Steve Majewski, for allowing me to finish this project before beginning a new one.

Table of contents

List of Figures

List of Tables

Chapter 1

PROJECT BACKGROUND

A galaxy is a collection of stars, and sometimes gas and dust, which is gravitationally bound together and forms the basic building block of large-scale structure in the universe. Galaxies come in three basic types: elliptical, spiral, and irregular. These types vary in their appearance, composition, and dynamics. With regard to dynamics, galaxies and their components can display complicated motions. For example, the centers of barred spiral galaxies contain stars that together make up a larger figure, the bar, which is elongated and can rotate, yielding a time-dependent, non-axisymmetric potential. This motion, called the figure rotation or pattern speed of a galaxy, is defined as the angular velocity at which a composite system or part of it rotates. This rotation is often comparable to that of a rigid body. For the purposes of this project, we wish to investigate the figure rotation of an elliptical galaxy.

1.1 Dynamics of Elliptical Galaxies

Studies of elliptical galaxies before the 1970's were based on assumptions we now know to be inaccurate. Among these are the notions that these objects are oblate spheroids, flattened by rotation, and that they are dynamically quiescent. Over time, these and several other elliptical galaxy "myths" were proven wrong.

An elliptical galaxy is to first order a collisionless, spheroidal stellar system in which two-body relaxation is much larger than a Hubble time (de Zeeuw & Franx 1991). Luminous giant ellipticals are in general dynamically hot:

$$\left(\frac{v_{max}}{\sigma_c}\right)^* \leq 1 \,, \tag{1.1}$$

where v_{max} is the maximum rotation velocity of the system and σ_c is the central velocity dispersion ("*" indicates a normalization based on the galaxy's ellipticity). For low luminosity ellipticals this fraction is about one, but for more luminous systems the fraction can be much lower than unity. Thus, for luminous elliptical systems, rotation is generally negligible compared to random motions. Rather than being rotationally supported, giant elliptical galaxies are supported by the pressure provided by their rather large (and possibly anisotropic) velocity dispersion component. The slow rotation of elliptical galaxies we observe leads us to believe that violent relaxation is not complete (Sparke & Gallagher 2000). The stars have not yet relaxed and may be far from an equilibrium state. This view of ellipticals is thus far from the simple systems we once thought them to be.

In determining the dynamics of elliptical galaxies, one can also derive information on the mass-to-light ratio M/L of the stellar populations. The M/L of a galaxy can be determined both independently of and as a function of specific mass models. To first order, the M/L can be simply derived from the virial theorem, if one assumes the galaxy to be in equilibrium, spherical, and nonrotating (Faber 1979). The following are used to find the total mass in the system:

$$M < V^2 > + \Omega = 0 \tag{1.2}$$

and

$$\Omega = -G \int_0^R \frac{M(r)\, dr}{r^2} \,, \tag{1.3}$$

where M is the total mass of the object, R is the total radius, $M(r)$ is the mass

contained within a sphere of radius r , and $< V^2 >$ is the mass-weighted average of the square of the stellar velocities (Poveda 1958; Faber 1979). This last quantity can be estimated from σ_c. From the empirical de Vaucouleurs $R^{1/4}$ relation, we have the following:

$$I(R) = I_e \, exp(-7.67[(R/R_e)^{1/4} - 1]) \; , \tag{1.4}$$

where R_e is the effective radius and I_e is the surface luminosity at R_e (de Vaucouleurs 1948; Binney & Merrifield 1998). From here, M/L can easily be found (Binney 1982):

$$M/L = \frac{0.201 \, \sigma_c^2}{G I_e R_e} \; . \tag{1.5}$$

Yet, it has been discovered that the properties of many galaxies depart significantly from the assumptions above and thus more flexible approaches must be used.

First, relating a galaxy's surface brightness and velocity dispersion profiles to its M/L is also possible through specific models, which make assumptions that depart from those above. For example, fitting the spherical and isotropic King Model to the center of an elliptical system, one can determine the central surface brightness I_o and the apparent core radius R_c:

$$I(R) = \frac{I_o}{1 + (R/R_c)^2} \; . \tag{1.6}$$

If σ_c is known, one can determine M/L through (Binney 1982)

$$M/L = \frac{9 \, \sigma_c^2}{2\pi G I_o R_c} \; . \tag{1.7}$$

Second, one of the most useful tools in studying elliptical galaxies is the fundamental plane. There exists several correlations between the known properties of elliptical

systems. First suggested were two-parameter correlations: the color-magnitude relation, the surface brightness-effective radius relation, the Faber-Jackson (luminosity – velocity dispersion) relation, etc. (Binney & Merrifield 1998). For example, from the Faber-Jackson relation, we can find the total luminosity of a galaxy L using σ_c (Faber & Jackson 1976):

$$L \propto \sigma_c^n \quad \text{, where} \quad 3 \leq n \leq 5 \quad \text{(observed)} \; . \tag{1.8}$$

This correlation is remarkably tight for a wide range of luminosities (Binney 1982). Yet for many of the two-parameter correlations there exists significant scatter that cannot be explained simply by measurement errors (Binney & Merrifield 1998), and it was discovered that the residuals from the different correlations are related. This lead to the construction of a three-parameter fundamental plane. Simply put, the two-parameter correlations are really projections of a three-dimensional plane. The fundamental plane can largely be explained by the virial theorem and is independent of detailed M/L models: $R_e \propto I_e^{-1}$. Departures from the expected fundamental plane can then be assigned to M/L variations, non-homologous or non-equilibrium behaviors.

Studies of elliptical dynamics must also deal with the concept of triaxiality. Triaxial galaxies contain three axes of different characteristic sizes. The stellar density of a simple triaxial galaxy can be described by

$$\rho(\vec{x}) = \rho(m^2), where \quad m^2 = \frac{x^2}{A^2} + \frac{y^2}{B^2} + \frac{z^2}{C^2} \quad \text{is a constant-density-surface,} \tag{1.9}$$

$\vec{x}$ is the position vector, and x, y, z are the short, middle, and long axes ($A > B > C$)

(Sparke & Gallagher, 2000). Using surface photometry, triaxiality can and has been detected in many galaxies (e.g. through isophotal twists). Yet the most compelling evidence that triaxiality is fairly common in elliptical systems comes from dynamical models and N-body simulations reproducing observations (Varnas et al. 1987; Merritt 1999).

When studying triaxiality, one must carefully consider the orbital structure of the stellar component. Many orbital families and shapes exist for triaxial potentials. For example, the following 2D elongated toy potential produces box, loop, and chaotic orbits (Figure 1.1):

$$\Phi(x,y) = \frac{1}{2} v_c^2 \, ln \left[R_c^2 + x^2 + \frac{y^2}{q^2} \right] , \tag{1.10}$$

where v_c is related to the circular velocity at large radii, R_c is a core radius, and q is a measure of the potential elongation.

In discussing the dynamics of triaxial elliptical galaxies, one of the most important subjects still to be explored is figure rotation. Figure rotation has important consequences for the orbital structure and may help to explain the survival of the steep nuclear cusps observed in elliptical galaxies (de Zeeuw & Franx 1991). This is because box orbits, which presumably support triaxiality, will avoid the center and thus the central cusp or black hole. In Binney's (1982) article on elliptical galaxies, some of the unanswered questions include: a) what are the pattern speeds of triaxial spheroidal systems?, and b) how do these speeds relate to the observed streaming motions within elliptical galaxies and the bulges of disk galaxies? de Zeeuw & Franx (1991) state that relatively little work has been done on triaxial galaxy models with figure rotation. Amazingly, this fact has not changed much in the last 14 years. While triaxial models

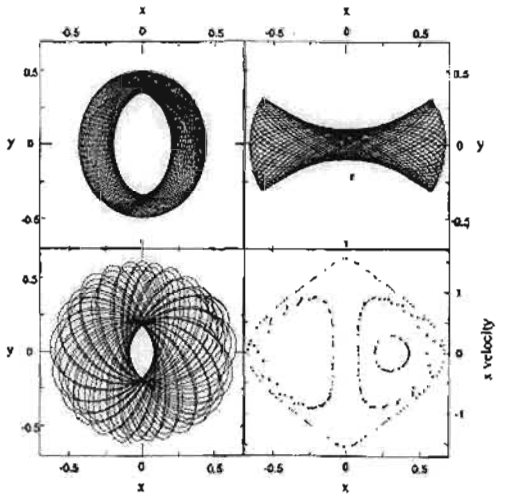

Fig. 1.1.— Loop (top left), box (top right), and chaotic (bottom left) orbits in a 2D elongated potential. The bottom right panel shows a surface of section for all three orbits (taken from Sparke & Gallagher 2000).

with figure rotation show promising results, there is a strong need for observational evidence of figure rotation.

But determining figure rotation observationally is challenging. The mostly featureless surface brightness profiles of elliptical galaxies suggest that their figure rotation must be quite small (Binney 1982). If the pattern speeds were large, the transfer of angular momentum at the associated resonances would presumably be more efficient, leading to morphological features such as those seen in barred spiral galaxies. Yet rapid advances in technology have made the subtle detection of elliptical figure rotation more and more realistic. With time, the questions that remain regarding triaxial galaxies and figure rotation should be answered. We provide a first attempt in this thesis.

1.2 Measuring Velocities in Galaxies

Since much of the kinematical information astronomers have concerning galaxies comes from the light emitted by stars, it is important to first understand how one can extract this information from a single star. Observed stellar spectra are generally blackbody spectra with absorption lines superimposed, and the nature of these absorption lines depends on the conditions at the photosphere of the star, such as temperature, chemical composition, surface gravity, etc.

Along with the physical characteristics of stars, absorption lines provide a great deal of information about stellar kinematics. The Doppler effect causes the absorption lines in stellar spectra to shift to shorter wavelengths (higher frequency) or longer wavelengths (lower frequency) as an object is moving towards or away from the observer. Using the measured offset, called the Doppler shift, the velocity along the observer's line-of-sight can be determined. If a given absorption line appears $\Delta\lambda$ away from its rest wavelength λ, then the velocity of the object can be derived using the following formula:

$$\frac{\Delta\lambda}{\lambda} = \frac{v}{c} , \tag{1.11}$$

where v is the line-of-sight velocity and c the speed of light. With respect to the specific spectral feature measured, a "spectral velocity" u can also be calculated:

$$u \equiv c ln\lambda . \tag{1.12}$$

Using this relation,

$$v = \frac{c\,\Delta\lambda}{\lambda} = c\,\Delta ln\lambda = \Delta u . \tag{1.13}$$

Thus, the change in the spectral velocity of a feature, Δu, equals the line-of-sight velocity of an object v (Binney & Merrifield 1998).

We now assume that the light we receive from galaxies is the sum of all its parts, that is, the sum of all the stars' light. Collectively, each star in a galaxy is moving towards or away from the observer at roughly the same line-of-sight velocity. This is referred to as the systemic velocity of the galaxy. However, since stars also have ordered and random motions, the velocities along the line-of-sight are slightly different for each star. This creates shifted and broadened spectral features in the spectrum of the galaxy, as shown in Figure 1.2.

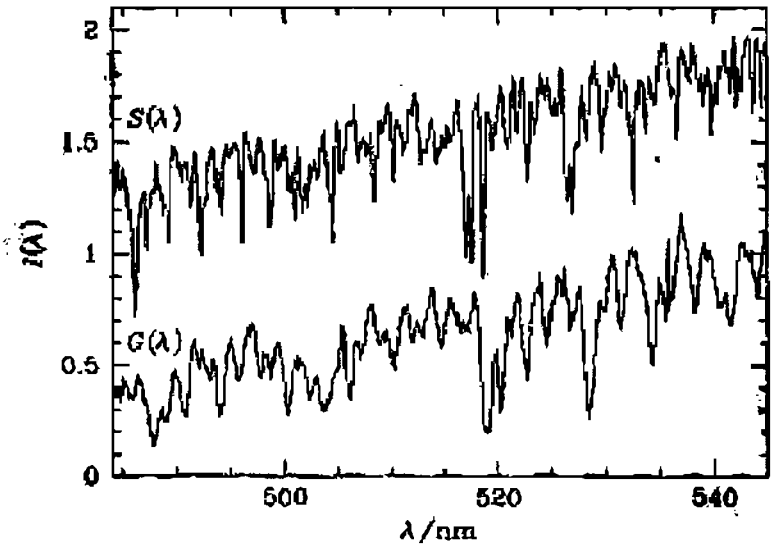

Fig. 1.2.— Taken from Binney & Merrifield (1998), these optical spectra, around the Mg b absorption feature at 518 nm, are of a K0 giant star (top) and the center of the lenticular galaxy NGC 2549 (bottom). Note the subtle differences between the K0 star absorption lines and the shifted and broadened spectral lines contained in the galaxy spectrum.

To recover the stellar kinematics, one must assume that the stars in a galaxy are all of the same type or can be described by a composite template that represents well the galaxy's stellar population mix. For example, it is known that elliptical galaxies contain mostly old G or K dwarf stars, while the disks of spiral galaxies, which often contain star forming regions, have younger stars. Although this assumption simplifies our problem, it can also create a major error, called template mismatch. In reality, galaxies are made up of many different types of stars and our assumption of one (effective) stellar type can cause biases in the stellar kinematics (see below). To avoid this, the template spectrum should be built from as many different stars as are known to reside in the galaxy.

To analyze the broadening of spectral lines due to stellar motions, one can define $F(v)$, the line-of-sight velocity distribution (LOSVD), where the fraction of stars with line-of-sight velocities between v and $v + dv$ is defined as $F(v)dv$. If we assume that all the stars in the galaxy have roughly the same spectrum $S(u)$ (the template), we can thus use the following equation to obtain $F(v)$:

$$G(u) \propto \int dv F(v) S(u - v) \ , \tag{1.14}$$

where $G(u)$ is the galaxy spectrum (Binney & Merrifield 1998). Simply put, this is the convolution of the template spectrum by the LOSVD.

There are several methods available to extract the LOSVD from the previous equation. The simplest of these is to take its Fourier transform. This results in the following expression:

$$\tilde{F}(\kappa) \propto \frac{\tilde{G}(\kappa)}{\tilde{S}(\kappa)} \ , \tag{1.15}$$

where $\sim$ denotes a Fourier transform and κ is the variable used to describe the velocity in Fourier space. While this method is very straightforward, it has several inherent problems, especially at low and high frequencies due to noise, errors in the continuum slope of the spectra, and finite spectral resolution. This has lead researchers to improve upon this original method, resulting in techniques such as the Fourier Quotient method (Sargent et al. 1977), the cross-correlation method (Simkin 1974), the stellar auto-correlation method (Franx & Illingworth 1988), and the Fourier Correlation Quotient method (Bender 1990).

The Fourier Quotient method (Sargent et al. 1977) assumes that the LOSVD has a Gaussian form described by the following equation:

$$F_{mod}(v \mid \bar{v}, \sigma) \propto exp\left[-\frac{(v-\bar{v})^2}{2\sigma^2}\right] , \tag{1.16}$$

where $\bar{v}$ is the mean line-of-sight velocity and σ the velocity dispersion.

Taking the Fourier transform of the LOSVD, we arrive at

$$\tilde{F}_{mod}(k \mid \bar{v}, \sigma) = \gamma exp\left[-\frac{1}{2}(2\pi\sigma k)^2\right] , \tag{1.17}$$

where γ is a normalization factor. By fitting $\tilde{F}_{mod}$ to $\tilde{F}$, one can solve for γ, $\bar{v}$, and σ. Like the basic Fourier method, this technique can produce erroneous results at high and low frequencies and is sensitive to template mismatch. Another disadvantage lies in the choice of F_{mod}. There is little reason to assume that the LOSVD is Gaussian. In fact, stars in the solar neighborhood have shown evidence of non-Gaussian velocity dispersions (Binney & Merrifield 1998). While this can be a major setback,

some methods that represent the LOSVD as sum of Gaussians have had success, such as the Unresolved Gaussian Decomposition (UGD) technique (Kuijken & Merrifield 1993).

The cross-correlation method takes the cross-correlation of the galaxy spectrum with the template spectrum (Simkin 1974):

$$CCF(v) = \int duG(u)S(u-v) \ . \tag{1.18}$$

By fitting a Gaussian to the result of this integral, one can determine $\bar{v}$ from the peak and σ from the width of the distribution (Figure 1.3). However, this method is also plagued by template mismatch and can be sensitive to instrumental broadening. To deal with the latter of these two problems, it is possible to simply subtract in quadrature the instrumental width directly from the velocity dispersion. However, this unsophisticated correction may cause more harm than good if neither the galaxy's broadening function nor the instrumental profile are truly Gaussian.

Related to the cross-correlation method is the stellar auto-correlation method (Franx & Illingworth 1988):

$$ACF(v) = \int duS(u)S(u-v) \ . \tag{1.19}$$

Taking the cross-correlation of the template spectrum with itself, this method uses the fact that the cross-correlation function (CCF) is simply the convolution of the auto-correlation function (ACF) with the LOSVD. Thus, $F(v)$ can be obtained from the deconvolution of the ACF from the CCF. The advantage of this method over the previous two is that it is non-parametric. Instead of assuming that the LOSVD

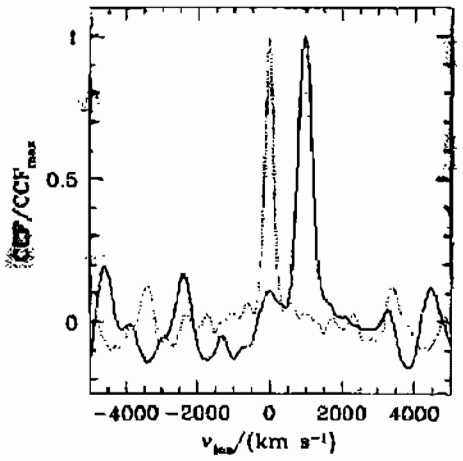

Fig. 1.3.— The cross-correlation function of a galaxy and a stellar spectrum (solid line) and the auto-correlation function of a stellar spectrum (dotted line), normalized to the peak values (Binney & Merrifield 1998).

is a Gaussian, no assumption is made. Working with correlation functions rather than with spectra also allows us to vary the parameters ($\bar{v}$, σ) until the best match is found between the observed galaxy spectrum and the convolution of the stellar template with the LOSVD.

1.2.1 Fourier Correlation Quotient Method

A far more reliable method, which will be used in this project, is the Fourier Correlation Quotient method (FCQ) (Bender 1990). This technique combines the Fourier quotient method with the stellar auto-correlation method. It is ideal for determining the velocity distribution along the line-of-sight because it combines the advantages of the two techniques while avoiding the common assumption that the velocity distribution is Gaussian.

To begin, the stellar template and galaxy spectra are described by the following expressions:

$$S(u) = \sum_m \alpha_m L(u - u_m) \tag{1.20}$$

and

$$G(u) = \int F(u - v) \left(\sum_m \beta_m L(v - u_m) \right) dv \ , \tag{1.21}$$

where α_m and β_m are line strengths, $L(u)$ is the instrumental profile for an unresolved line, and u_m is the position of the m^{th} line. FCQ requires calculating the template-galaxy correlation function $K_{S,G}(v)$, followed by the autocorrelation function of the template star $K_{S,S}(v)$:

$$K_{S,G}(v) = \int G(u + v) S(u) du \tag{1.22a}$$

$$= \sum_{m,n} \alpha_m \beta_n \left(\int F(v - u) L(v - u_n) L(v - u_m - u) dv du \right) \tag{1.22b}$$

and

$$K_{S,S}(v) = \int S(u + v) S(u) du \tag{1.23a}$$

$$= \sum_{m,n} \alpha_m \alpha_n \int L(v - u_n) L(v - u_m - u) dv \ . \tag{1.23b}$$

Similarly,

$$\tilde{K}_{S,G}(\kappa) = \sum_{m,n} \alpha_m \beta_n e^{i\kappa(u_n - u_m)} \tilde{F}(\kappa) \, \tilde{L}^*(\kappa) \, \tilde{L}(\kappa) \tag{1.24}$$

and

$$\tilde{K}_{S,S}(\kappa) = \sum_{m,n} \alpha_m \alpha_n e^{i\kappa(u_n - u_m)} \tilde{L}^*(\kappa)\, \tilde{L}(\kappa) \ , \tag{1.25}$$

where $\tilde{L}^*(\kappa)$ is the complex conjugate of $\tilde{L}(\kappa)$. Using the ordinary Fourier Quotient method then gives the following equation:

$$\frac{\tilde{K}_{S,G}(\kappa)}{\tilde{K}_{S,S}(\kappa)} = \frac{\sum_n \beta_n e^{i\kappa u_n}}{\sum_m \alpha_m e^{i\kappa u_m}} \tilde{F}(\kappa) \ . \tag{1.26}$$

However, by deconvolving the peak of the template-galaxy correlations with the peak of the template autocorrelation, the above can be simplified:

$$\frac{\tilde{K}_{S,G,peak}(\kappa)}{\tilde{K}_{S,S,peak}(\kappa)} = \frac{\sum_m \alpha_m \beta_m}{\sum_n \alpha_n \beta_n} \tilde{F}(\kappa) \propto \tilde{F}(\kappa) \ . \tag{1.27}$$

From this final equation, the broadening function $F(u)$ can be recovered in a way that is largely independent from template mismatch.

1.2.2 Gauss-Hermite Series

Regardless of the deconvolution method chosen, the objective usually is to find the first few moments of the LOSVD, defined as

$$\mu_k = \int dv (v - \bar{v})^k F(v) \ , \tag{1.28}$$

where the mean velocity is

$$\bar{v} = \int dv v F(v) \ , \tag{1.29}$$

and the velocity dispersion is

$$\sigma \equiv \sqrt{\mu_2} \ . \tag{1.30}$$

Calculating higher order moments tells us about the shape of the LOSVD. For example, the coefficients of skewness ζ_3 and kurtosis ζ_4 are related to the moments of the LOSVD via

$$\zeta_k \equiv \mu_k / \sigma^k \ . \tag{1.31}$$

While the skewness describes the profile's departure from central symmetry, the kurtosis measures symmetric departures from a pure Gaussian.

Fitting a truncated Gauss-Hermite series to the LOSVD, one can easily obtain measurements of all four quantities (van der Marel & Franx 1993; Gerhard 1993). Here we adopt the following parameterization:

$$F_{GH} \propto e^{-\frac{1}{2}w^2} \left[1 + \sum_{k=3}^{n} h_k H_k(w) \right], \quad \text{with } n = 4 \text{ only} \ , \tag{1.32}$$

where $w = (v - \bar{v})/\sigma$, h_k are constant coefficients, and $H_k(w)$ are the Hermite polynomials of order k. By fitting $\bar{v}$, σ, h_3, and h_4 to the LOSVD, one obtains a robust description of the observed galaxy spectrum. Furthermore, given the exponential factor in Eq.1.32, this method is less susceptible to the wings of the LOSVD, which are usually badly constrained by the observations. This procedure is thus more reliable than calculating the true moments of the LOSVD directly, while the best-fit parameters obtained remain directly related to the true moments and offer the same physical insight into the galaxy dynamics (e.g., $\zeta_3 \propto h_3$, $\zeta_4 \propto h_4$; van der Marel & Franx 1993; see also Figure 1.4). This procedure is now commonly used in stellar kinematic studies.

1.3 The Tremaine-Weinberg Method

The Tremaine-Weinberg (1984) method was designed to measure the pattern speed of barred spiral galaxies, i.e., disk objects. For this project, we will attempt to use this method to measure the figure rotation of NGC 5266, an elliptical galaxy of approximately known geometry. Previously, this pattern speed, i.e. the angular velocity with which the pattern rotates, could not be directly measured observationally. Instead, numerical simulations were carried out in a model-dependent way to match the observations, and the pattern speed extracted from the best fitting model. With the TW method, the pattern speed can be calculated using only observed measurements of position, velocity, and surface brightness, leading to more direct, model-independent measurements.

The TW method in its simplest form relies on three assumptions (Tremaine & Weinberg 1984): 1) the disk of the galaxy is flat, 2) the object has a well-defined and unique pattern speed, and 3) the surface brightness of the tracer obeys the continuity equation. This first assumption ensures that the geometry of the galaxy is well known and that there is no vertical streaming motions. Most important, the galaxy's line-of-nodes, where the disk and sky planes intersect, must be accurately determined. It is along this direction that the velocity and position measurements are taken. Large errors in the pattern speed can result if the line-of-nodes is even slightly off (Debattista 2003). The second assumption simply ensures that a single pattern exists across the entire galaxy, and that it is stable. For the pattern speed to be measurable, the chosen tracer must rotate at a constant angular speed and its surface brightness must

be describable by the equation

$$\Sigma(x, y, t) = \Sigma(R, \phi - \Omega_p t) \ , \tag{1.33}$$

where t is the time, Ω_p is the pattern speed, and (x,y) and (R,ϕ) are the usual Cartesian and polar coordinates in the disk plane. Finally, the last and most important assumption requires that the luminosity density of the tracer obeys a continuity equation with no source or sink terms. In practice, the total mass of the tracer should remain fixed and the apparent luminosity per unit mass must be constant over a timescale of order a dynamical time:

$$\frac{\partial \sum(x, y, t)}{\partial t} + \frac{\partial}{\partial x}\left[\sum(x, y, t) v_x(x, y, t)\right] + \frac{\partial}{\partial y}\left[\sum(x, y, t) v_y(x, y, t)\right] = 0 \ , \tag{1.34}$$

where v_x and v_y are the mean velocities of the tracer. For spiral galaxies, this requirement of continuity is often not met for the gas, which may rapidly change phase through the conversion of neutral gas to molecular or ionized gas or vice-versa. On the other hand, this is often an accurate assumption if the tracer consists of stars that are unlikely to change their constitution rapidly and the object is dust-free.

Using the inclination, surface brightness distribution, and velocity field, one can then obtain the pattern speed as follows (Tremaine & Weinberg 1984):

$$\Omega_p \sin i = \frac{\int_{-\infty}^{\infty} h(Y) dY \int_{-\infty}^{\infty} \Sigma(X, Y)(v(X, Y) - v_o) dX}{\int_{-\infty}^{\infty} h(Y) dY \int_{-\infty}^{\infty} \Sigma(X, Y)(X - X_o) dX} \ , \tag{1.35}$$

where i is the inclination, (X, Y) are Cartesian coordinates in the plane of the sky (X

must be parallel to the line-of-nodes, i.e. along the major-axis if the disk is circular), X_o is the center of the galaxy, v_o is the systemic velocity of the galaxy, and $h(Y)$ is an arbitrary weighting function. The most useful weighting function are odd in Y (e.g. $h(-Y) = -h(Y)$), so as to cancel zeropoint errors in position or velocity.

A simpler and more robust version of this equation for use with slit spectroscopy is as follows (see Merrifield & Kuijken 1995):

$$\Omega_p \sin i = \frac{< v > - v_o}{< X > - X_o} , \tag{1.36}$$

where the brackets represent luminosity-weighted averages along slits and can be obtained by simply collapsing the slit data along the spatial (for $< v >$) and dispersion (for $< X >$) directions and determining the mean.

This method is more robust than naively applying Eq.1.35 since the two measurements have much higher signal-to-noise ratio (S/N) than the numerous measurements required by Eq.1.35. In addition, if one has multiple slits at a given orientation (each at a different offset Y), then the slope of a linear fit to $< v >$ vs. $< X >$ will yield $\Omega_p \sin i$ unaffected by zero-point errors in velocity or position (i.e. it is not necessary to know or measure v_o and X_o, as long as the same zero-points are adopted for all offset slits).

While Tremaine & Weinberg (1984) argue for the reliability of their method's application to spiral systems, we wish to apply the same technique to triaxial ellipticals. But before doing so, the three assumptions and requirements stated in the beginning must be re-evaluated. To begin with, the line-of-nodes of a prospective galaxy must be es-

tablished. For spiral galaxies, this is simply the position angle of the outer disk. But, this is not necessarily the case for elliptical systems, where the geometry is unknown and probably triaxial. Yet, if the elliptical galaxy in question contains a minor-axis dust lane, then the geometry can be approximately constrained. Assuming that the minor-axis dust lane identifies one of the two planes of symmetry where gas is stable, the line-of-nodes may be interpreted as lying close to the apparent major axis of the galaxy. This argument is strengthened if the galaxy displays rapid rotation along this same axis.

The second assumption of a well-defined pattern speed is probably also valid for elliptical systems. Contrary to the disks of spirals, the stellar components of ellipticals are unlikely to be able to support independent/secondary and/or transitory patterns (such as flocculent spiral arms), which may have an independent pattern speed. However, if ellipticals do form mainly through accretion of smaller systems, the resulting torques may not allow the establishment of a steady figure rotation. Nevertheless, through theoretical models, tumbling elliptical systems embedded in triaxial potentials have been shown to exist and be stable (Merritt 1999). Furthermore, the survival of steep nuclear cusps may be explained through rotating triaxial potentials. Thus far, none of this has been proved observationally, but for this project we will assume that elliptical systems do have figure rotation (even if small), and that this quantity can be measured using the TW method. From other studies of figure rotation of cosmological dark matter halos, we can expect values ranging from 0.1 to 8.0 $\mathrm{km\,s^{-1}\,kpc^{-1}}$ for elliptical systems (Bailin & Steinmetz 2004).

The third assumption deals with the validity of the continuity equation. Most ellip-

tical galaxies lack the young blue stars (indicative of star formation) and obscuring dust and cool gas that characterize spiral systems. Proof of this can be found in the typical spectrum of an elliptical galaxy, where the broadened and shifted features resemble the spectra of K and M giant stars (see Figure 1.2). While spiral galaxies contain much neutral hydrogen and molecular gas that may be converted into stars, the stellar content of elliptical galaxies is much less likely to change rapidly with time.

Considering these three assumptions, there are three potential problems to apply the TW method to elliptical systems. First, elliptical galaxies are not two-dimensional, flat objects. Any net vertical motion could potentially ruin our measurements. Second, we must acknowledge that the galaxy we wish to study in this project contains a minor-axis dust lane. While giving clues to the galaxy's geometry, dust can be problematic when applying the TW method, masking part of the tracer and breaking the continuity requirement. Third, the precise measurement of the line-of-nodes position angle is also problematic. For elliptical galaxies, only an approximate value is available without detailed dynamical modeling.

Keeping the above warnings in mind, we now argue why NGC 5266 is a good candidate for this project.

1.4 NGC 5266: A Minor-Axis Dust-Lane Elliptical Galaxy

NGC 5266, shown in Figure 1.6a, is a fast-rotating E4 minor-axis dust lane elliptical galaxy. Unlike most ellipticals, NGC 5266 contains a perpendicular ring of dust and an inner ionized gas disk that lack a substantial population of stars (Varnas et al. 1987). Galaxies of this type are of interest to astronomers because they offer key information about their geometry, which is essential for determining their 3D dynamics. The goal of this project is to use the Tremaine-Weinberg method to measure or constrain the pattern speed of NGC 5266. This would represent the first such measurement in any elliptical and will shed light on the applicability of the method to these systems.

Although NGC 5266 is classified as an S0 galaxy in William Herschel's New General Catalog, it is more likely an E4 elliptical. Not only do the isophotes show that this galaxy fits the Hubble type E4, but the surface brightness profile is also well described by the $R^{1/4}$ law (Caldwell 1984). Varnas et al. (1987) showed that for this galaxy, the best-fit parameters (using a GG 385 filter) are μ_e = 23.80 mag $arcsec^{-2}$ and R_e = 65", where μ_e is the effective surface brightness.

Using the results from photometric studies, one can determine the orientation of the galaxy's major and minor axes. Fitting ellipses to the isophotes has shown that the major axis of NGC 5266 lies at a PA of 107°, while the minor axis lies at a PA of 17° (Varnas et al. 1987). Analysis of the spectra confirms that the stars within the galaxy rotate rapidly about the minor axis, with a maximum rotation velocity of 212 ± 7

km s^{-1} (Varnas et al. 1987). NGC 5266 is thus one of the fastest rotating elliptical galaxies known today. There is also a slow stellar rotation about the major axis of 43 ± 16 km s^{-1}, strongly suggestive of a triaxial shape (Varnas et al. 1987). The gas associated with the dust lane rotates at 260 ± 10 km s^{-1}, in retrograde motion with respect to the stars, suggesting that this material has an external origin (Varnas et al. 1987). In the north-northeast region of the galaxy, the outer dust lane also contains a warp and the gas motions associated with this warp are prograde with respect to the stellar rotation about the major axis (Caldwell 1984). It has been suggested that a warped disk in a quasi-settled configuration, such as the one in NGC 5266, is caused by the triaxial figure of NGC 5266 tumbling in an opposite direction to the observed stellar streaming (Varnas et al. 1987).

NGC 5266 is unique because of its substantial outer dust lane and inner ionized gas disk, both of which lie in the plane of the apparent minor axis. The ionized gas disk most likely formed from gas that originated in the outer dust lane and then drifted towards the galaxy center, where it was ionized by shock heating or a central continuum source (Caldwell 1984). The dust lane and warped gas disk are probably remnants of a massive gas-rich spiral galaxy that was captured into a polar orbit (Varnas et al. 1987). There is however no strong evidence that the warped disk is a result of incomplete settling, which may be important to discriminate between studies in which the warps of galaxies such as NGC 5266 are interpreted as stationary or transient phenomena (see van Albada et al. 1982, Bertola et al. 1985).

HI observations of NGC 5266 show the neutral gas to be very extended along a PA of 135° (Morganti et al. 1997; see Figure 1.7a). This is perpendicular to the dust lane,

a fact that is unusual for a galaxy such as this. A position-velocity map at this same PA shows the HI to occupy three distinct components: a fast-rotating component associated with the dust lane, a main HI disk, and two outermost arm structures that may be associated with tidal arms or an outer, edge-on disk or ring (see Figure 1.7b). Modelling these observations results in NGC 5266 containing two orthogonal HI disks with a constant rotation velocity of $270\,\mathrm{km\,s^{-1}}$ out to a radius of 4' from the center. These results suggest that NGC 5266 is the product of the merger of two gas-rich spiral galaxies that occurred roughly 1.2 Gyr ago.

Studies of triaxiality in NGC 5266 show that this galaxy is most likely 5 to 10% triaxial and 90 to 95% oblate (Caldwell 1984; Varnas et al. 1987). Elliptical galaxies are in general described as spherical, prolate, oblate, or triaxial spheroids. NGC 5266 is thus probably in between an isotropic oblate system and a strongly triaxial system (Varnas et al. 1987). But while Caldwell (1984) uses the angle of the warp in the outer dust lane to estimate the triaxiality of NGC 5266, Varnas et al. (1987) argue that this method cannot be used to estimate a lower limit for the triaxiality. Instead, they construct models of the disk and compares the results with observations. Both groups nevertheless obtain similar results, with Caldwell's (1984) method producing a triaxiality of 5% and Varnas et al. (1987) creating a best-fit model with 10% triaxiality.

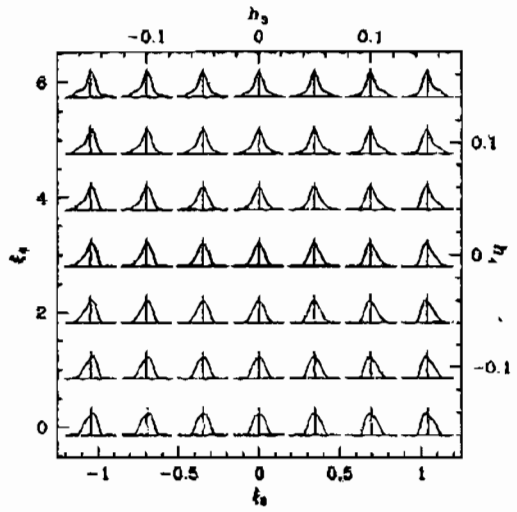

Fig. 1.4.— Diagram depicting nearly Gaussian velocity distributions and their dependence on skewness ζ_3 and kurtosis ζ_4. Note the pure Gaussian at the center and the relationship between h_3, h_4 and ζ_3, ζ_4, respectively (Binney & Merrifield 1998).

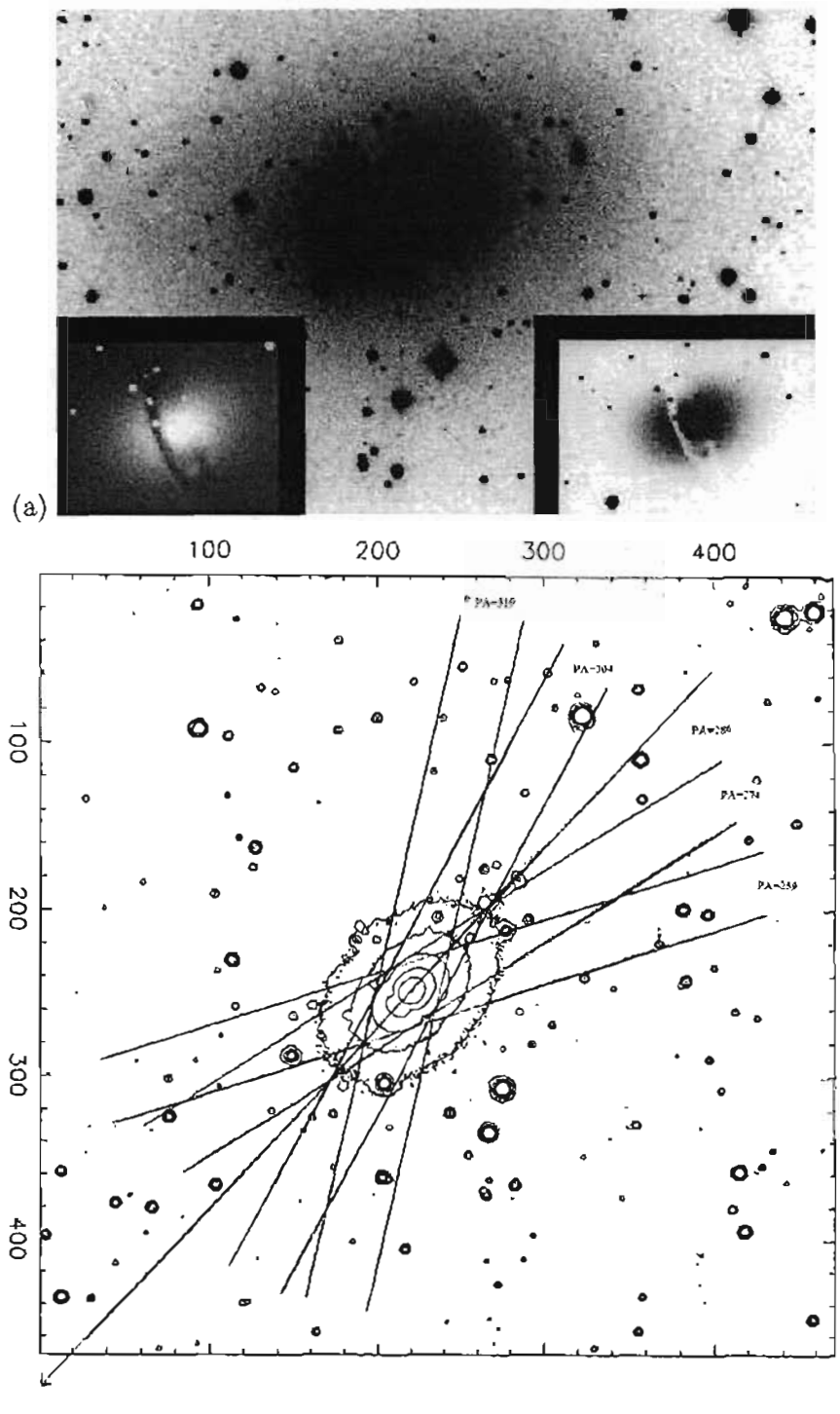

Fig. 1.5.— (a) Optical images of NGC 5266. In the left and right inserts, note the elongated shape of the galaxy, consistent with its high rotation, and the inner minor-axis dust lane (Sandage & Bedke 1994). (b) Contour plot of NGC 5266 with the major axis at a PA of 289° labeled and PA=259° ± 11″, 274° ± 11″, 304° ± 11″, and 319° ± 11″ slits overlaid.

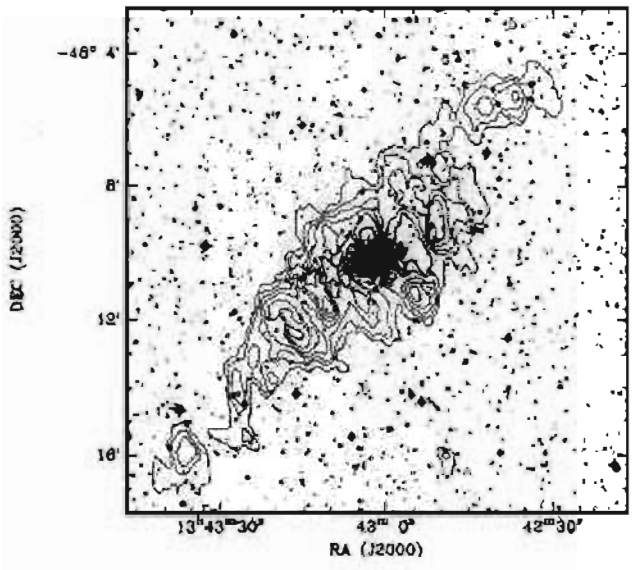

(a)

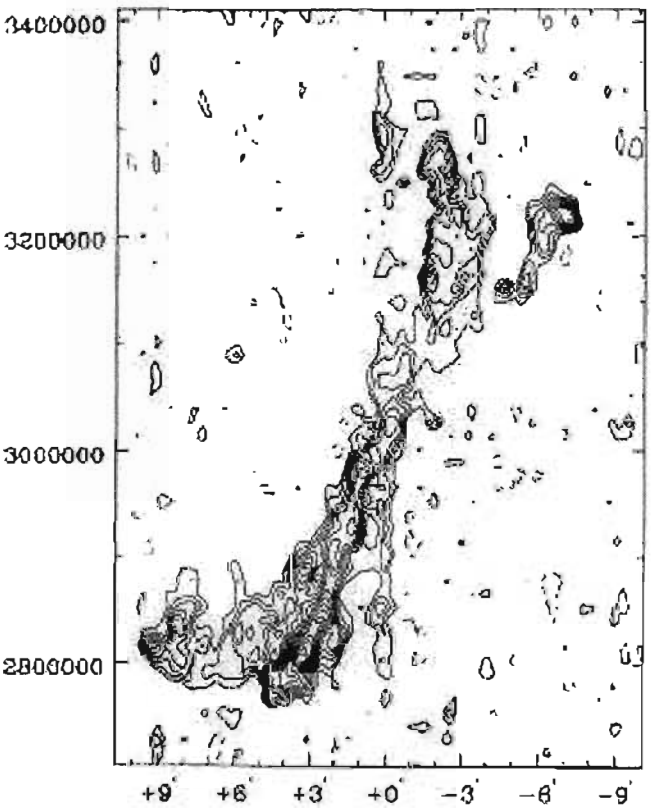

(b)

Fig. 1.6.— (a) Total HI distribution in NGC 5266 superimposed on an optical image from the Sky Survey. (b) Position-velocity map at a PA of 135°, with a width of 90″. Contour levels range from -11.11 to 80 mJy beam^{-1} with steps of 6 mJy beam^{-1} (both figures taken from Morganti et al.)

Chapter 2

DATA REDUCTION

2.1 Data Acquisition and Reductions

The observations of NGC 5266 were acquired by Dr. Martin Bureau and Dr. Ken Freeman on April 7-8 1997 and May 10-13 1997 using the 2.3 meter telescope at Siding Spring Observatory, Australia (Figure 2.1). Working with the Double Beam Spectrograph (DBS; Figure 2.2), red and blue optical long-slit spectra covering approximately 950 Å were obtained simultaneously, using a grating of 1200 lines mm^{-1} on both arms and a slit roughly 6.′7 long. The red spectra were centered on the Hα line at 6563 Å while the blue spectra were centered on the Mgb triplet at 5170 Å. The spatial sampling of the spectra is 0.″9 pix^{-1} and the dispersion 0.55 Å pix^{-1}, yielding a two-pixel spectral resolution of 1.1 Å. The readout noise in the images is typically 4–5 e^- while the gain is 1 e^-ADU^{-1}.

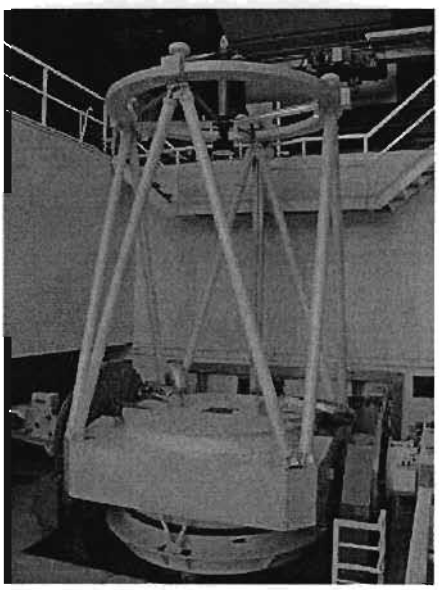

Fig. 2.1.— The 2.3-meter telescope at Siding Spring Observatory, Australia.

For this project, each of the six nights of observing consisted of taking bias frames,

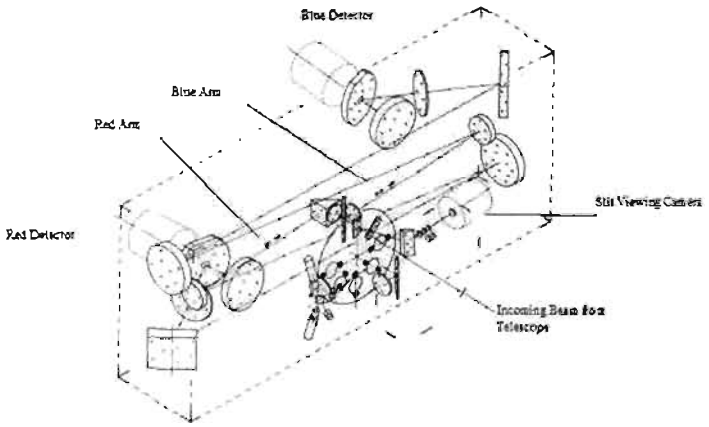

Fig. 2.2.— Optical components of the Double Beam Spectrograph. Note the location of the red and blue arms and detectors (Rodgers, Conroy, & Bloxham 1988).

quartz-iodine continuum lamp flats, neon-argon (NeAr) arc spectra bracketing science exposures, sky flats, template star spectra, and spectra of NGC 5266 itself. The spectra are in a two-dimensional, long-slit format, with the dispersion running approximately along the x-axis (columns) and the spatial direction roughly along the y-axis (rows). For NGC 5266, a total of 63 red spectra and 67 blue spectra of 2000 seconds each were obtained. Some images were corrupted or had particularly bad bias levels, leaving 55 red spectra and 62 blue spectra. The data were taken at four position angles (PA's): 259°, 274°, 304°, and 319° (± 15° and ± 30° from the major-axis of NGC 5266 at 289°). For data at PAs of 259°, 274°, and 304°, offsets along the minor-axis of 0″, −11″, and +11″ were used. Cloudy weather and bad seeing prevented taking spectra at a PA of 319° and an offset of −11″. An attempt was made to obtain spectra using an offset of +22″ at a PA of 274°, but the S/N reached was too low. No spectrum was taken along the major axis (PA = 289°), since as can be seen from Eq. 1.35 the TW method fails if the figure is aligned with the line-of-nodes

(X axis). A breakdown of the valid spectra obtained is shown in Table 2.1.

The data reduction was carried out using the Image Reduction and Analysis Facility (IRAF; Tody 1986). The reduction was completed in roughly 20 steps, with the red and blue spectra analyzed separately. The April and May data were also treated separately due to small differences in the methods of observation.

2.2 Bias Correction

The virtual overscan region in each of the images must first be subtracted. While the red and blue charge coupled devices (CCDs) are 1752 x 532 pixel^2, the recorded images were 1852 x 562 pixel^2 for April and 1852 x 632 pixel^2 for May. The extra pixels are virtual overscan regions, which provide an estimate of the bias level and readout noise simultaneously with the image. By examining several lamp flats, the data and virtual overscan sections of the images were first determined. Using the "colbias" and "linebias" routines, the medians of the overscan regions along the spatial and dispersion axes were then successively subtracted. The overscan regions are discarded and the images trimmed at the same time.

Because of remaining low-level, large-scale bias structures in the images, it is still necessary to produce and subtract a "master" bias constructed from 0 s exposures. While this "master" bias subtraction was done for the May data, the bias frames from April were of a poor quality and could not be used. For illustrative purposes, Figure 2.3 shows two images before bias subtraction, while Figure 2.4 shows a "master" bias frame.

Table 2.1. List of two-dimensional spectra of NGC 5266 obtained from the red and blue arms of the Double Beam Spectrograph.

PA (degrees)	Offset (arcsecs)	Number of Exposures	Total Exposure Time (s)
		RED	
259	0	5	10000
259	+11	4	8000
259	-11	6	12000
274	0	5	10000
274	+11	6	12000
274	-11	4	8000
304	0	5	10000
304	+11	4	8000
304	-11	6	12000
319	0	5	10000
319	+11	5	10000
319	-11	0	0
		BLUE	
259	0	5	10000
259	+11	4	8000
259	-11	6	12000
274	0	5	10000
274	+11	6	12000
274	-11	5	10000
304	0	7	14000
304	+11	5	10000
304	-11	6	12000
319	0	6	12000
319	+11	7	14000
319	-11	0	0

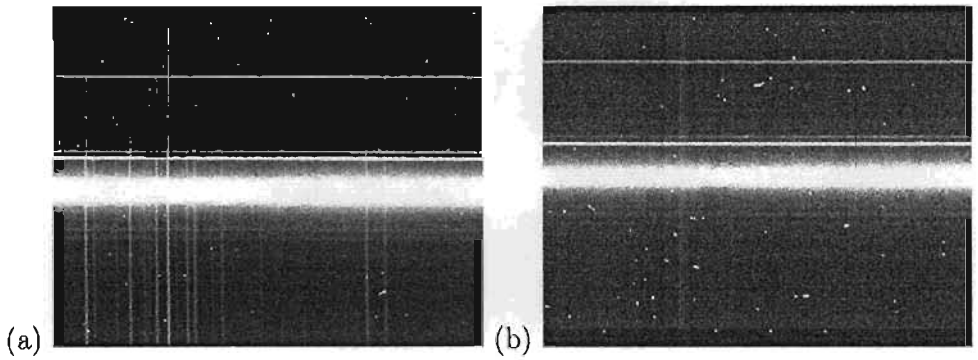

Fig. 2.3.— Red (a) and blue (b) spectrum of NGC 5266 at PA=274° and zero offset. Hereafter, all figures will be of NGC 5266 at these specifications and only the central portion of the blue spectrum will be shown.

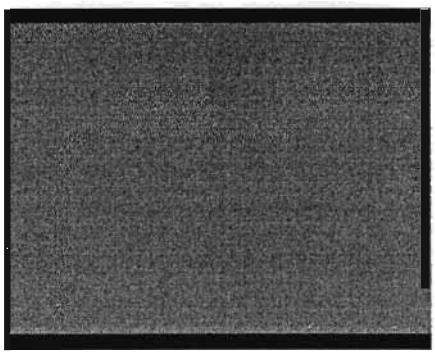

Fig. 2.4.— "Master" bias constructed from 0 s exposures taken during the May run.

2.3 Dark Subtraction

Generally, the next step is to subtract the dark current, caused by free electrons generated through thermal effects. However, on most modern CCDs, this current is negligible compared with the readout noise of the detector once cooled to low temperatures. Since this was the case for our data, it was not necessary to perform any dark subtraction.

2.4 Flat-Fielding

In order to remove pixel-to-pixel sensitivity variations caused by the inhomogeneous quantum efficiency of the detector, and to some extent by small-scale vignetting and other instrumental effects, one needs to produce and divide the data by a "master" flat. Several flats were taken each night using a quartz-iodine continuum lamp, producing a smooth illumination across the CCD. Once this smooth variation is removed, the remaining fluctuations are directly related to variations in the detector's sensitivity.

Flat-fielding the data requires five steps: 1) producing a master flat, 2) flattening the master flat along the dispersion axis, 3) flattening the master flat along the spatial axis, 4) smoothing the flat further in both directions (if necessary), and 5) dividing each data frame by the resulting, flattened master flat. The flat frames from each day were first combined together (Figure 2.5a) and the task "response" used to remove smooth gradients along the dispersion and spatial axes (Figures 2.5b – 2.5c), using only low-order fits (here cubic spline functions with each order corresponding to roughly 50 pixels). This somewhat flattened "master" flat still contains large-scale variations of order 3 – 5 %, requiring further flattening with "imsurfit" (Figure 2.5d). This fits a 2D function and results in a better master flat with acceptable variations of less than 0.5 %. The final step in flat-fielding the data is to divide all images by the final, flattened master flat.

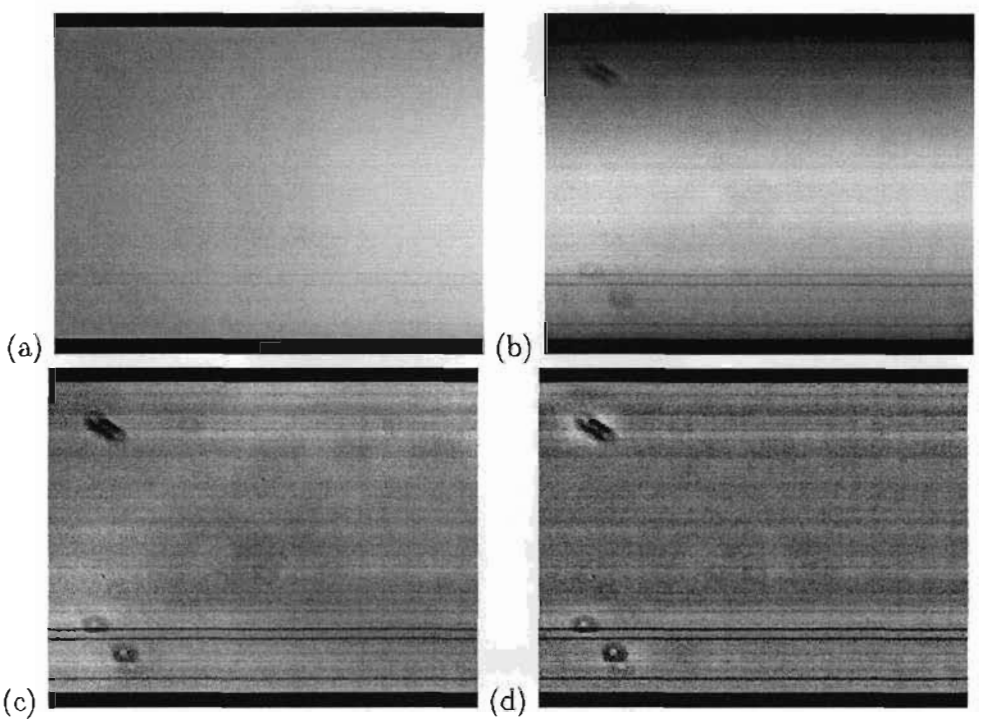

Fig. 2.5.— Various stages in the creation of a master flat. (a) Master flat created from quartz-iodine lamp exposures. (b) Master flat flattened in the dispersion direction using "response". (c) Master flat flattened in the spatial direction also using "response". (d) Final master flat after using "imsurfit". The donut-shaped marks on the flats are most likely caused by dust on the dewar window, while the three horizontal lines at the bottom are probably due to dirt on the slit.

2.5 Tilt Correction

Following the flat-fielding, the next step is to measure and correct for the tilt in the spectra, so that later in the reduction the dispersion axis lies exactly along the x-axis. This is done by simply measuring the y-position of a continuum source in each frame for at least two positions along the dispersion axis, and then rotating all frames by an average value.

2.6 Line Identification

For the next series of steps, the arc spectra are calibrated, traced, and fit. The arc spectra are created using a neon-argon (NeAr) lamp with a characteristic spectrum (Figure 2.6) and the numerous emission lines are used to calibrate the wavelength scale of the galaxy, template star, and sky spectra. Using the interactive tasks "identify" and "reidentify", a few strong emission lines are first identified by hand (Figure 2.7a), the remaining lines are identified automatically from a preliminary fit and line list (Figure 2.7b), and all lines are then traced along the spatial axis. This is done for every arc spectrum on all days, making it possible to precisely map the function λ(x,y) in all spectra.

Following "reidentify", a two-dimensional fit of $\lambda(x, y)$ is made to all identified lines and traces using "fitcoords" (here a chebyshev function is used, with x and y orders equal to 6).

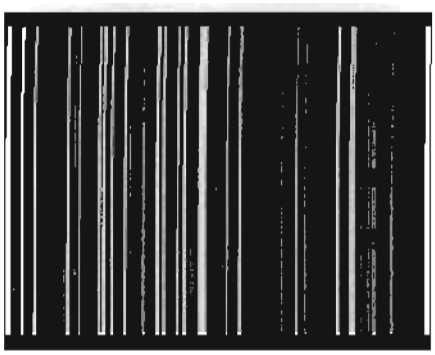

Fig. 2.6.— 2D NeAr arc spectrum.

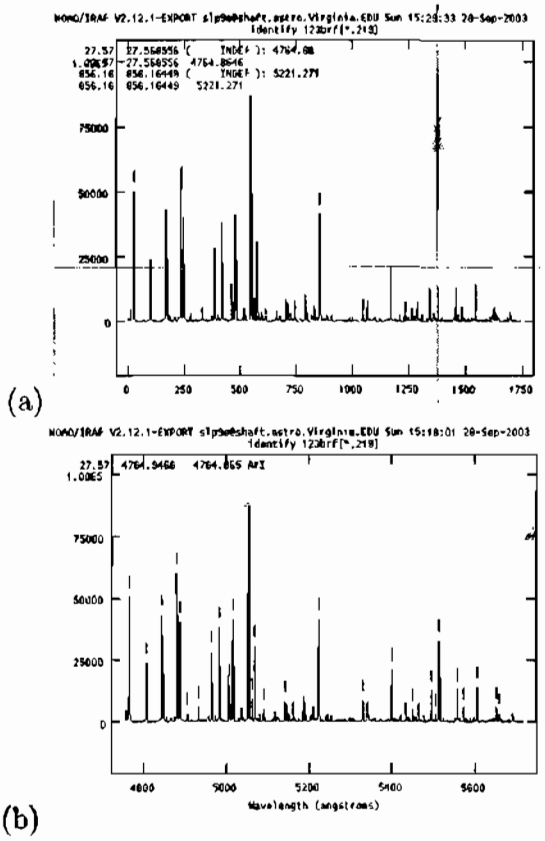

Fig. 2.7.— (a) NeAr spectrum before the completion of "identify". Note the emission lines identified by hand. (b) NeAr spectrum after all the emission lines have been identified.

2.7 Coordinate Transformation

At this stage, it is now possible to convert the dispersion axis from pixel units to those of wavelength, using the NeAr arc fits taken before and after each object spectrum (galaxy, template star, sky) and the task "transform".

It is possible to determine the approximate velocity sampling of our data using the Doppler equations (Eq.1.11-1.13) and the spectral sampling (0.55 Å pix^{-1}). For Hα redshifted by 3074 $\mathrm{km\,s}^{-1}$ (the systemic velocity of NGC 5266), this yields 25

$km\,s^{-1}\,pix^{-1}$ for the red arm and 32 $km\,s^{-1}\,pix^{-1}$ for the blue arm. Using these values, along with the start and end wavelengths obtained from "fitcoords", the galaxy, template star, and sky frames can all be transformed to a logarithmic wavelength (linear velocity) scale.

The sky lines in the transformed data frames can be examined to determine if and how the peak location and full width at half maximum (FWHM) change along the spatial direction. Using this information, one can tell if a) the lines are tilted or curved and the wavelength calibration has failed or b) the slit focus differs from one end of the slit to the other.

2.8 Illumination Correction

Next, it is necessary to create a "master" twilight sky flat that will be divided out from all galaxy and template star frames. All sky frames are first combined together, normalized at the spatial center, and then fit along the spatial directions, using large bins to avoid the effects of strong sky lines (here 20 pixels per bin along the dispersion axis and 10 pixels per bin along the spatial axis). The resulting fit is then divided into each object frame (Figures 2.8 – 2.9).

2.9 Combining Frames

At this point the images must be prepared for combining. During observations, the telescope is moved slightly along the slit after each exposure to remove CCD defects

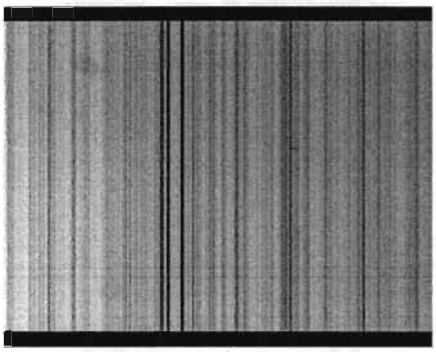

Fig. 2.8.— Master sky flat used for the illumination correction.

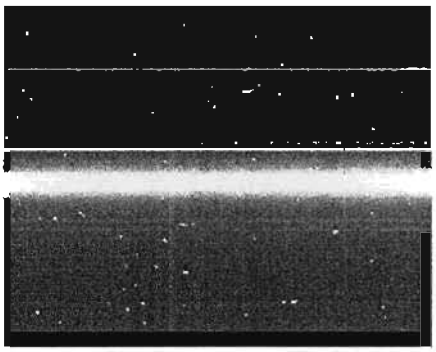

Fig. 2.9.— Blue spectrum after illumination correction.

when combining. By fitting the center of the continuum in each image, the exact location of the object along the slit can be determined and the image offsets calculated. In order to measure the shift needed in the dispersion (velocity) direction, one needs to calculate the necessary correction for the Earth's motion using "rvcorrect", to bring each frame to the heliocentric rest frame. The images can then be shifted and merged using "combine", scaling and weighting by the flux in each image. This is also crucial to eliminate cosmic rays (Figure 2.10).

The final reduction of the galaxy frames is described below. The template stars are reduced differently using "apall", as they must be extracted to a one-dimensional

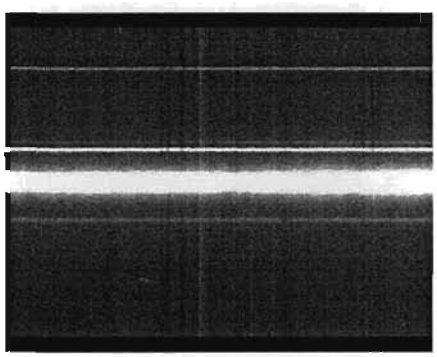

Fig. 2.10.— Blue spectrum of NGC 5266 after combining 4 spectra. Note that the cosmic rays and CCD defects have now disappeared and the S/N has increased.

form (the galaxies must remain in a two-dimensional format).

2.10 Background Subtraction

As each object frame contains signal not only from the object but also from background sources such as moonlight, reflected sunlight, and atmospheric emission lines, it is necessary to remove the background sky emission. We remove this signal using "background", a linear fitting function, and two emission-free regions on either side of the object along the slit. While this works well for most sky lines, some lines are very strong and their subtraction is not perfect. Depending on how bad the subtraction is, and the location in the spectra, one can either interpolate over or truncate the problematic regions (Figure 2.11).

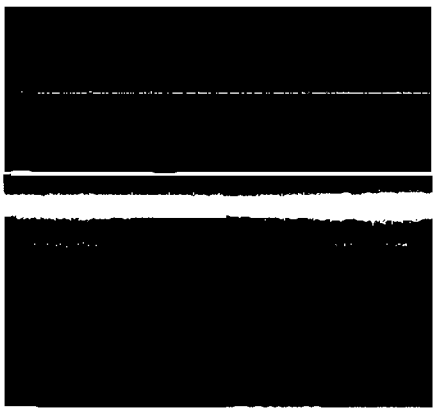

Fig. 2.11.— Blue spectrum of NGC 5266 after sky subtraction.

2.11 Subtraction and Normalization of Continuum

While the previous background fit and subtraction is done along the spatial direction, further analysis requires either subtracting or normalizing the continuum along the dispersion axis. For the red arm data, where we are mostly interested in the ionized-gas kinematics and thus the emission lines, the stellar continuum is subtracted using "background" (here with a cubic spline fit of order 17, or $\approx$ 100 pixels per order). The final red images cover the spectral range $\lambda 6065 - 7012$ Å (April) and $\lambda 6138 - 7083$ Å (May) (Figure 2.12a). For the blue spectra, where we are mostly interested in stellar kinematics and thus the absorption lines, we instead normalize the continuum using "continuum" (and subtract one to have a mean continuum level of zero). The final blue images are cover $\lambda 4779 - 5743$ Å (April) and $\lambda 4752 - 5715$ Å (May) (Figures 2.12b).

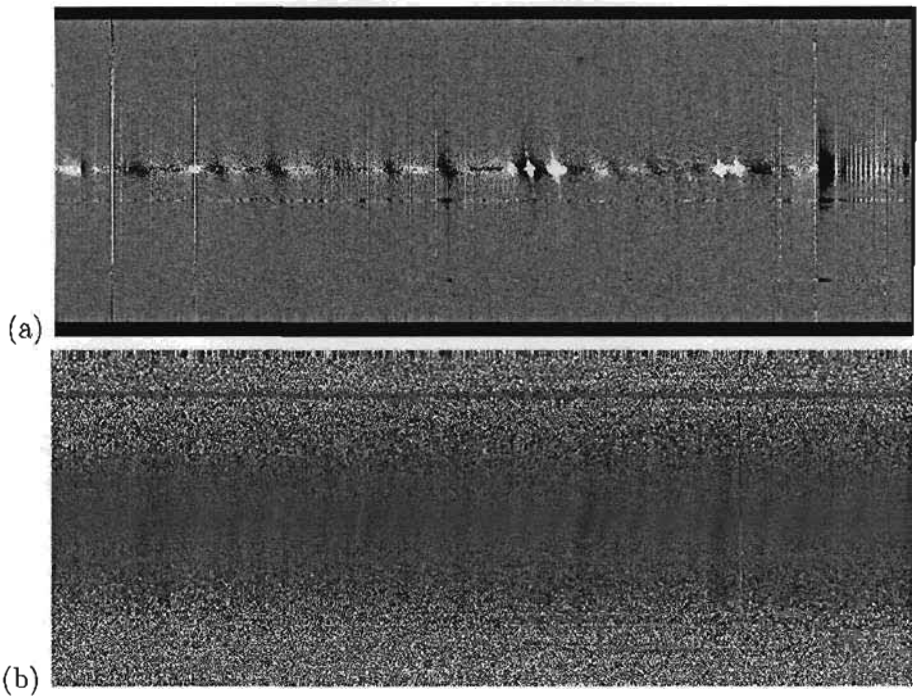

Fig. 2.12.— (a) The entire final red spectrum of NGC 5266 at a PA of 274° and an offset of 0". One can see several galactic absorption and emission lines, as well as badly subtracted sky lines. (b) The entire final blue spectrum of NGC 5266 at a PA of 274° and an offset of 0". The original image has been trimmed and the stretch has been changed so that absorption lines can been seen more easily.

2.12 Extraction of Stellar Spectra

For the several template stars observed, the interactive task "apall" was used to extract one-dimensional spectra from the original two-dimensional long-slit data. This involves finding the center of the stellar profile in the spatial direction and establishing the limits of the extraction aperture and sky regions (Figure 2.13). By separating the stellar spectra by day, 12 template star spectra were created, six for each observing run. These, along with the galaxy spectra, were then processed in the steps described in Chapter 3 to extract the stellar kinematics.

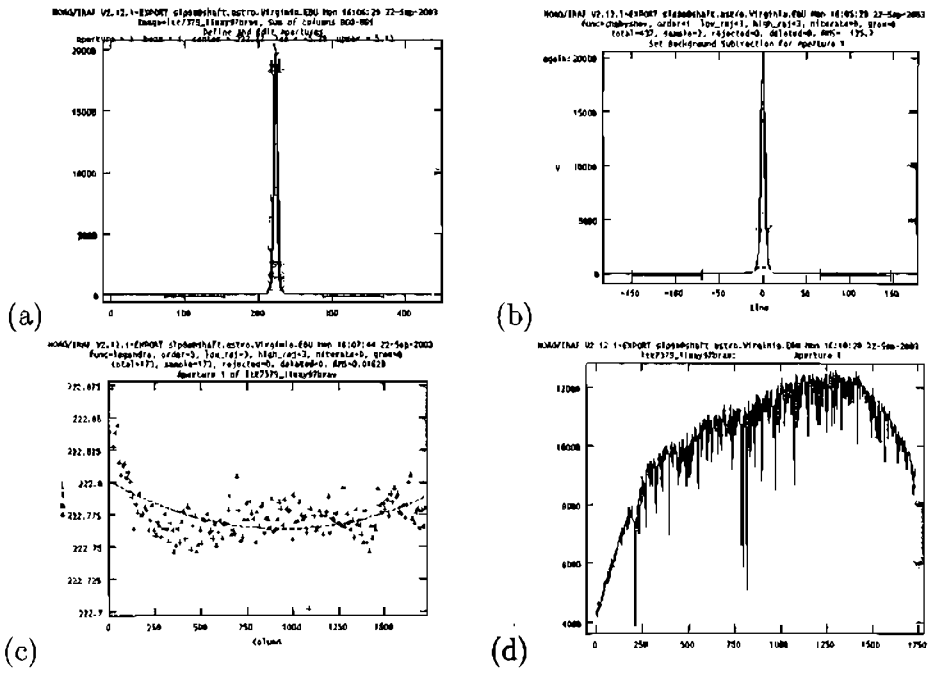

Fig. 2.13.— Various screen shots taken from the procedure "apall". (a) Stellar profile fitting. (b) Background fitting. (c) Tracing the spectrum along dispersion axis. (d) Extracted spectrum.

2.13 Finalization

While the standard data reduction steps are complete, there are two more steps that must be taken to ease the kinematic analysis. The first of these is to fix spectral regions containing badly subtracted sky lines. Fortunately, most of these lines occur at the ends of the spectra, away from where most of the lines of interest lie. One of the worst sky lines occurs at λ5577 Å in the blue spectra, due to OI emission line from the atmosphere. While Varnas et al. (1987) chose to remove this line through linear interpolation, we decided to truncate the last 200 or so pixels of each blue spectrum. A similar method was used to remove the numerous badly subtracted lines from the red end of the red spectra (see Figure 2.12a).

Next, it is important to center the galaxy in the spatial direction on the midpoint of a pixel, so that the spatial bins on each side of the center are symmetric. This will allow us to more easily determine the errors in our kinematic measurements (see Chapter 3).

Chapter 3

DATA ANALYSIS

To extract information on the ionized-gas and stellar kinematics of NGC 5266, one must separately analyze the red and blue spectra, respectively. The red spectra contain the strong and widely used emission lines of Hα λ6563 Å, [NII] λ6548, 6585 Å, and [SII] λ6717, 6731 Å, but no useful absorption lines. The blue spectra contain the weaker emission lines of Hβ λ4861 Å and [OIII] λ4959, 5007 Å and the strong absorption features of Mg b λ5170 Å, widely used for stellar kinematics. As our main interest for this project lies in the stellar kinematics, only the blue spectra will be used hereafter. The red spectra may be analyzed in future projects, which would allow for a more complete comparison of our observations to models of elliptical galaxies with minor-axis dust lanes.

Two types of galactic spectra are used for our analysis. The two-dimensional spectra before normalization are used for the TW calculations (see Figure 2.11), while one-dimensional spectra after normalization (obtained by slicing the 2D spectra along the spatial direction) are used to derive the stellar kinematics (e.g. Figure 3.1).

3.1 Weighted Signal-to-Noise Ratio (S/N) and Position Calculations

All stellar kinematic information can be extracted using the Fourier-Correlation Quotient (FCQ) method and the 1D spectra mentioned above. However, to obtain reliable results, the S/N of each spectrum must be above a certain minimum threshold. Thus in general, many spectra must be added together in the outer parts of the galaxy, requiring a reliable binning algorithm.

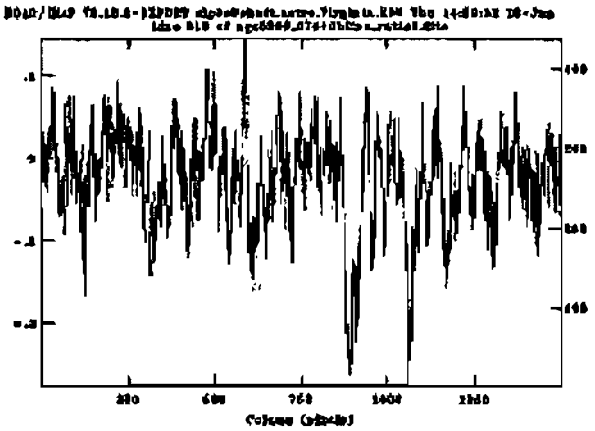

Fig. 3.1.— Central normalized blue spectrum of NGC 5266 at a PA of 274° and an offset of 0".

For this, a program was created to calculate and compare the S/N of each row (i.e. each 1D spectrum) of a two-dimensional spectrum with a chosen threshold, and bin rows together if required. Adopting a weighting inversely proportional to the variance of one-spectrum, the weighted signal of a sum of spectra is given by

$$S = \frac{\sum_{i=1}^{n} \frac{1}{\sigma_i^2} S_i}{\sum_{i=1}^{n} \frac{1}{\sigma_i^2}} \tag{3.1}$$

$$\approx 1 \quad \text{for} \quad S_i \approx \bar{S}_i \approx 1 \qquad \text{(appropriate for normalized spectra)}, \tag{3.2}$$

where n is the total number of rows added and $\bar{S}_i$ and σ_i^2 are the mean and variance in a given row defined in the standard manner:

$$\bar{S}_i = \frac{\sum_{j=1}^{m} S_{i,j}}{m} \tag{3.3}$$

$$\approx 1 \quad \text{by definition for normalized spectra}, \tag{3.4}$$

$$\sigma_i^2 = \frac{\sum_{j=1}^{m} (S_{i,j} - \bar{S}_i)^2}{m} \tag{3.5}$$

$$\approx \frac{\sum_{j=1}^{m} (S_{i,j} - 1)^2}{m} \quad \text{for} \quad \bar{S}_i \approx 1, \tag{3.6}$$

where m is the total number of pixels in row i and $S_{i,j}$ is the signal in pixel j of row i.

In calculating the variance, a 3σ cut-off is also used to exclude any remaining bad pixels. Using the same weighting and applying the standard error formula, the resulting noise is given by

$$N = \sqrt{\sum_{i=1}^{n} \left(\frac{1/\sigma_i^2}{\sum_{i=1}^{n} 1/\sigma_i^2} \right)^2 \sigma_i^2} \tag{3.7}$$

$$= \frac{1}{\sum_{i=1}^{n} 1/\sigma_i^2} \quad \sqrt{\sum_{i=1}^{n} \frac{1}{\sigma_i^2}} \tag{3.8}$$

$$= \frac{1}{\sqrt{\sum_{i=1}^{n} 1/\sigma_i^2}}. \tag{3.9}$$

The resulting S/N for a sum of spectra is thus

$$S/N = \frac{\sum_{i=1}^{n} \frac{1}{\sigma_i^2} S_i}{\sqrt{\sum_{i=1}^{n} \frac{1}{\sigma_i^2}}} \tag{3.10}$$

$$\approx \sqrt{\sum_{i=1}^{n} \frac{1}{\sigma_i^2}} \quad \text{for} \quad S_i \approx \bar{S}_i \approx 1. \tag{3.11}$$

For this project, the S/N of the central row is first calculated and compared to the adopted threshold. If the S/N is below the threshold, then the first rows above and below are combined and the S/N recalculated and retested. The binning continues until the S/N in the center exceeds the threshold given. Thereafter, the rows above and below the central row are checked and combined in a separate but symmetric manner, ensuring symmetric bins on both sides of the center.

Along with the S/N, the position of the binned one-dimensional spectra must also be recalculated to take into account the weight of the individual spectra. The mean (effective) position is then

$$\bar{x} = \frac{\sum_{i=1}^{n} \frac{1}{\sigma_i^2} x_i}{\sum_{i=1}^{n} \frac{1}{\sigma_i^2}}, \tag{3.12}$$

where x_i is the position of row i.

With the above procedures, for each slit position, we obtain several binned one-dimensional spectra and their mean position with respect to the center of the galaxy.

Table 3.1 summarizes the number of binned spectra produced for each slit and S/N threshold. Each binned spectrum yields a reliable and independent kinematic measurement (see next section). As expected, as the S/N threshold increases, fewer one-dimensional spectra are created for each slit. Furthermore, as all slit positions had similar exposure times (Table 2.1), the two-dimensional spectra with no offset generally yield more 1-d spectra than those with offsets of $\pm$ 11 arcseconds.

3.2 FCQ Method and LOSVDs

Using a single binned one-dimensional galaxy spectrum and a previously reduced template star spectrum, the FCQ method described in Section 1.2.1 yields the galaxy's LOSVD at that position, which is then fit using a Gauss-Hermite series to give v, σ, h_3, and h_4 (see Section 1.2.2). The programs used for this analysis come from the XSAURON software package used in the SAURON project (e.g. Bacon et al. 2001; de Zeeuw et al. 2002). The "*fcq*" and "*fit_losvd*" programs were respectively used to extract the LOSVD from the galactic spectrum and fit it.

After calculating v, σ, h_3, and h_4 for all the one-dimensional spectra of every slit, we averaged the results for the two bins symmetrically opposed on either side of the galaxy center (essentially folding the kinematic profiles). For σ and h_4 a direct average was used, while for v and h_3 the points differ by a sign change, as the latter quantities are expected to be anti-symmetric (odd) with respect to the galaxy center. The input values are also checked against both the average and neighboring points to throw away significantly deviant measurements. For every bin, the error on the average is taken to be half the difference between the two opposed measurements.

For the positions, the size of the bin defines the "error". Although it was thought that the dust ring would significantly affect the measurements, the kinematic profiles show that only a few points deviate significantly from the average around that region.

To aid the interpretation of the results, we also plot the light profile of the galaxy along each slit. For this, the continuum image (Figure 2.11) was simply collapsed in the dispersion direction and left uncalibrated. Both the original and folded values are plotted to clearly show the location of the dust lane.

As a test for template mismatch, each of the template stars was used to extract the stellar kinematics (two stars of type K1III and one star of type G0). When compared with one another, the results are consistent, so that template mismatch does not seem to be a problem. Having more diverse stellar types would however provide a more stringent test.

The resulting kinematic profiles along each slit are shown in Figure 4.1-4.4 and discussed in Chapter 4.

3.3 Applying the Tremaine-Weinberg Method

Using the simplified version of the TW method (Merrifield & Kuijken 1995; Eq.1.36), determining the pattern speed is fairly straightforward. There are two main steps involved: determining the mean position $< X >$ and determining the mean velocity $< v >$ for each PA and offset. The slope of a linear fit to $< v >$ vs. $< X >$ then yields $\Omega \sin(i)$, as long as the same position and velocity zero-points are adopted for

all offset slits of a given PA (but independent of them).

For the velocities, this is ensured by the fact that all data show the same wavelength (and thus velocity) calibration, and that all were processed with the same template star. However, when collapsing the data spatially, one must make sure to either symmetrically exclude or interpolate over foreground stars, which can bias the velocity measurements if bright enough.

For the positions, it is much harder to ensure consistent zero-points between different slits. This is because the galaxy may have been moved along the slit for different offsets and because, for triaxial systems, the maximum of the light profile along the slit may not follow the so-called Y-axis of the TW method. In other words, the photometric minor-axis need not be, and generally is not, perpendicular to the line-of-nodes and the PA adopted (this is most obvious for barred spiral galaxies). The only way forward is thus to determine $< X >$ with respect to the maximum of the light profile along the slit, and to i) calculate the offset between the latter and a fixed axis perpendicular to the line-of-nodes (the same for all offsets) using an image or ii) to assume that the latter is at a fixed angle with respect to the PA adopted and calculate the offset from there (note: method i) was chosen for this project). Again, however, one must either symmetrically exclude or interpolate over foreground stars when determining the mean position.

To determine the mean velocity $< v >$, we used the non-normalized two-dimensional blue spectra, which are collapsed in the spatial direction for each PA and offset, yielding $G_T(\mu)$, the integrated spectrum. This is then normalized as for the original

two-dimensional spectra and fed into "fcq", yielding $F_T(v)$, the integrated LOSVD along the slit. The luminosity-weighted mean velocity $< v >$ is then determined in the standard manner:

$$< v >= \frac{\sum_{j=0}^{m} v_j F_T(v_j)}{\sum_{j=0}^{m} F_T(v_j)}, \tag{3.13}$$

where m is the number of pixels along the LOSVD in the velocity direction.

To find the mean position $< X >$, we again used the non-normalized two-dimensional blue spectra. For each PA and offset, the spectra are collapsed in the dispersion direction, yielding $\Sigma(X)$, the luminosity profile along the slit. Foreground stars are corrected for when necessary and the luminosity-weighted mean position is again determined in the standard manner:

$$< X >= \frac{\sum_{i=0}^{n} X_i \Sigma(X_i)}{\sum_{i=0}^{n} \Sigma(X_i)}, \tag{3.14}$$

where n is the number of pixels along the slit in the spatial direction. For both $< X >$ and $< v >$ measurements, it is necessary in practice to limit the summations above to only part of the $\Sigma(X)$ and $F_T(v)$ profiles. Figures 3.2 – 3.12 show both the $\Sigma(X)$ and $F_T(v)$ profiles used in the calculations above. To obtain accurate results, one must use only the central portion of these profiles (assuming a monotonic decline), especially for $F_T(v)$. The other bumps and wiggles on either side of the main peak are spurious features and may bias the results.

The resulting plots of $< v >$ vs. $< X >$ for the different PAs are shown in Figures 4.5 – 4.8 and discussed in Chapter 4.

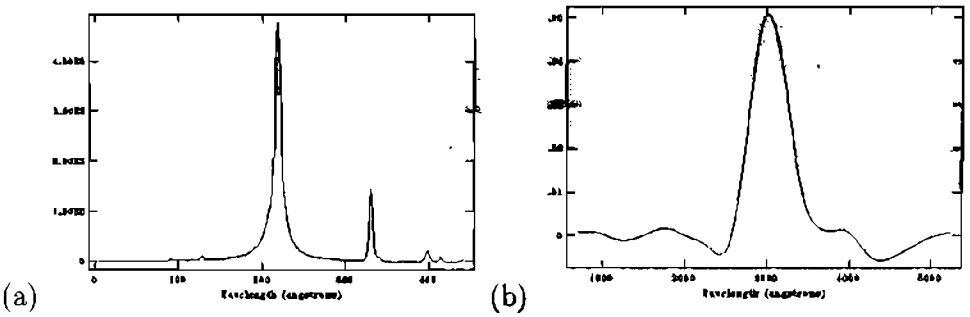

(a) (b)

Fig. 3.2.— Profile of $\Sigma(X)$ (left) and $F_T(v)$ (right) for NGC 5266 at PA = 259°, offset = 0″. Note that the x-axis of the $\Sigma(X)$ plots in Fig. 3.3 – 3.13 are incorrect. They should read "Position (pixels)". Also note that for plots of $F_T(v)$ in Fig. 3.3 – 3.13, the x-axis has been incorrectly labeled by IRAF as "Wavelength (angstroms)". It should read "v (km s^{-1})". Flux scales are linear but arbitrary.

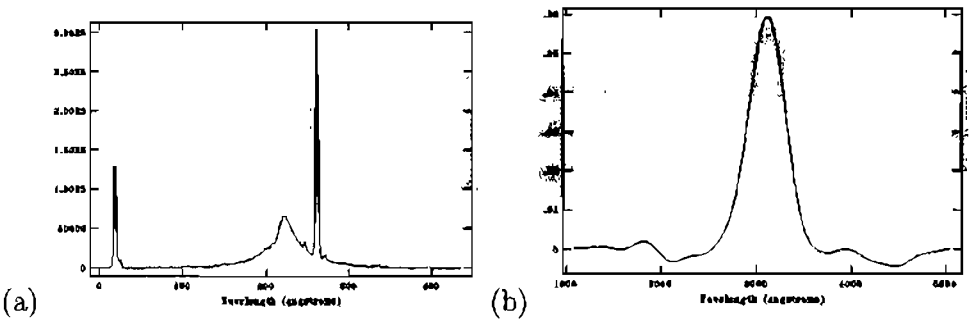

(a) (b)

Fig. 3.3.— Profile of $\Sigma(X)$ (left) and $F_T(v)$ (right) for NGC 5266 at PA = 259°, offset = +11″.

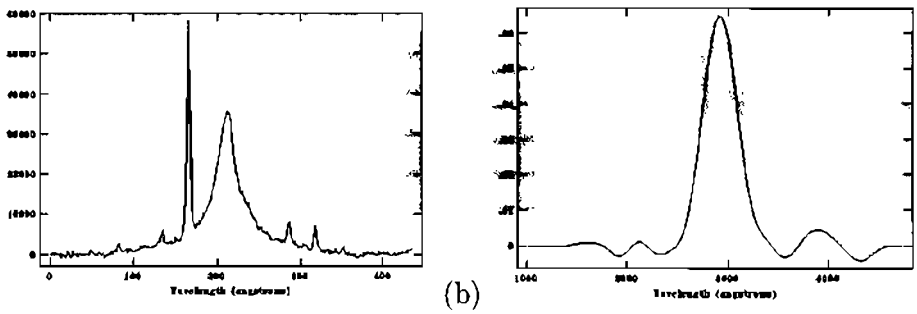

(a) (b)

Fig. 3.4.— Profile of $\Sigma(X)$ (left) and $F_T(v)$ (right) for NGC 5266 at PA = 259°, offset = $-11''$.

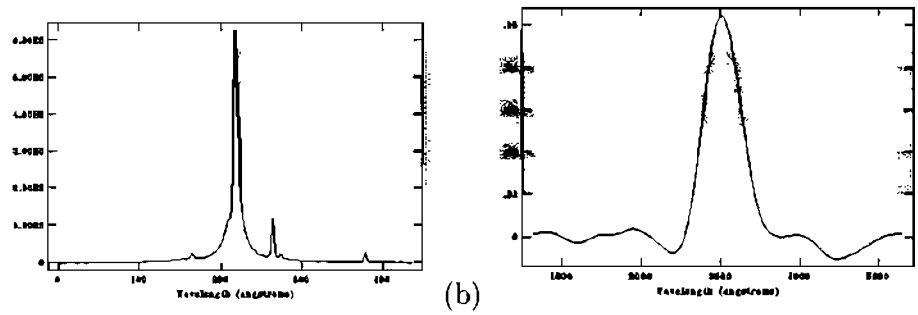

(a) (b)

Fig. 3.5.— Profile of $\Sigma(X)$ (left) and $F_T(v)$ (right) for NGC 5266 at PA = 274°, offset = $0''$.

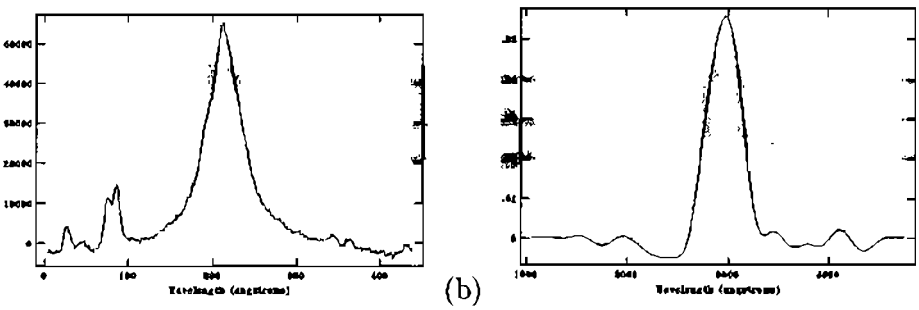

(a) (b)

Fig. 3.6.— Profile of $\Sigma(X)$ (left) and $F_T(v)$ (right) for NGC 5266 at PA = 274°, offset = $+11''$.

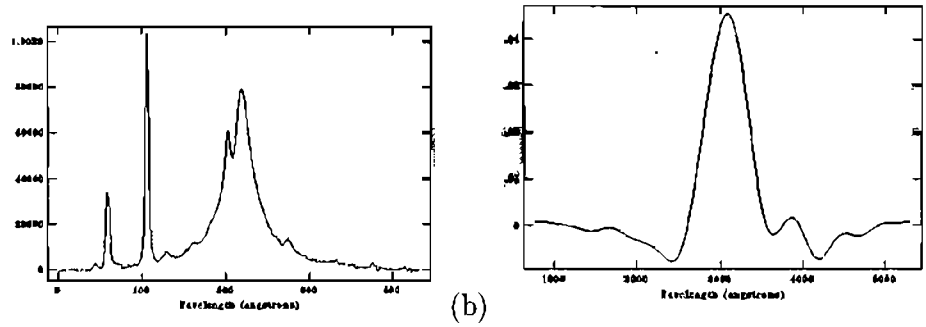

(a) (b)

Fig. 3.7.— Profile of $\Sigma(X)$ (left) and $F_T(v)$ (right) for NGC 5266 at PA = 274°, offset = $-11''$.

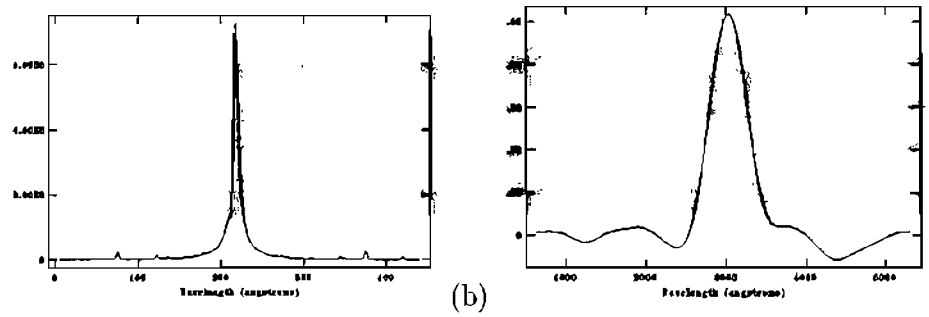

(a) (b)

Fig. 3.8.— Profile of $\Sigma(X)$ (left) and $F_T(v)$ (right) for NGC 5266 at PA = 304°, offset = $0''$.

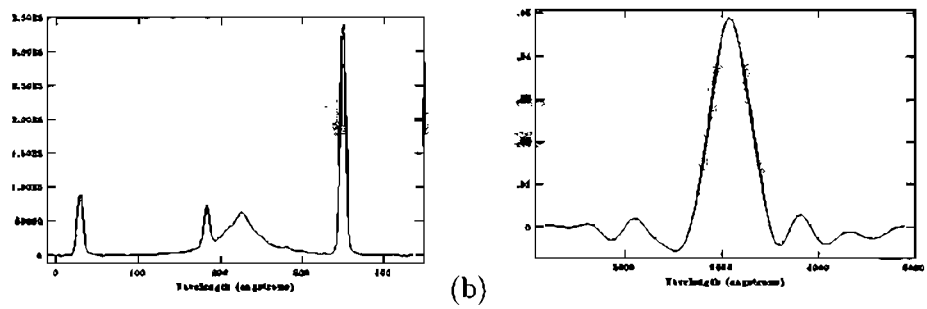

(a) (b)

Fig. 3.9.— Profile of $\Sigma(X)$ (left) and $F_T(v)$ (right) for NGC 5266 at PA = 304°, offset = $+11''$.

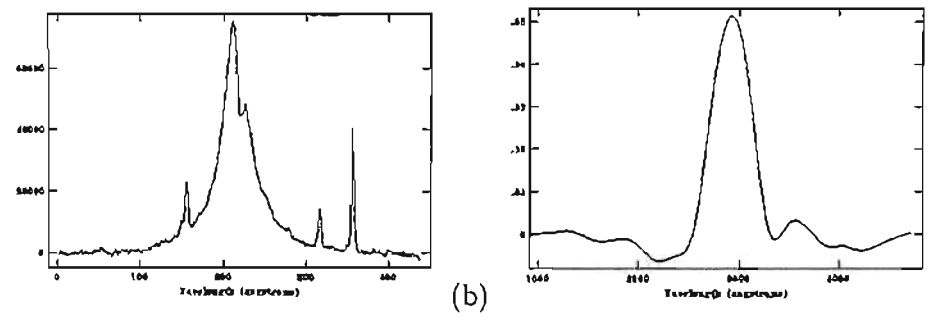

(a) (b)

Fig. 3.10.— Profile of $\Sigma(X)$ (left) and $F_T(v)$ (right) for NGC 5266 at PA = 304°, offset = $-11''$.

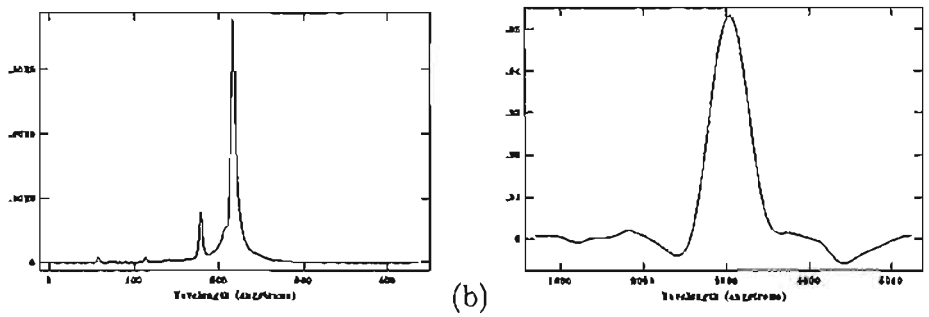

(a) (b)

Fig. 3.11.— Profile of $\Sigma(X)$ (left) and $F_T(v)$ (right) for NGC 5266 at PA = 319°, offset = $0''$.

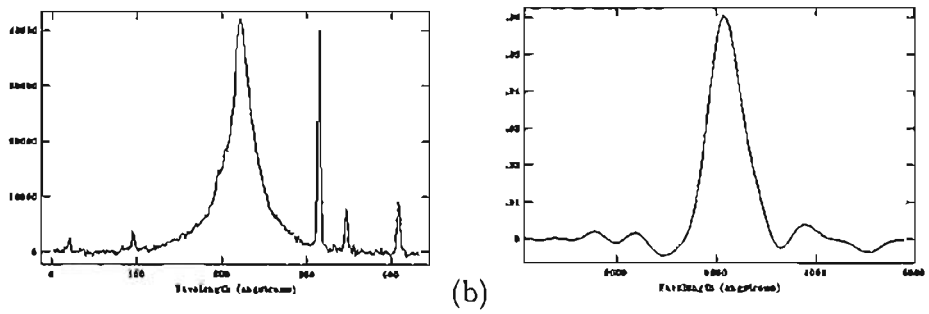

(a) (b)

Fig. 3.12.— Profile of $\Sigma(X)$ (left) and $F_T(v)$ (right) for NGC 5266 at PA = 319°, offset = $+11''$.

Table 3.1. One-dimensional NGC 5266 spectra: position angle, offset, and number of spectra produced for each signal-to-noise ratio threshold.

		Number of Spectra Produced			
PA (degrees)	Offset (arcsecs)	S/N=10	S/N=13	S/N=15	S/N=20
259	0	49	39	25	19
259	+11	23	17	13	7
259	-11	41	25	19	13
274	0	51	39	31	19
274	+11	59	43	31	19
274	-11	45	29	23	13
304	0	59	43	31	21
304	+11	43	27	23	13
304	-11	59	37	31	21
319	0	53	43	31	21
319	+11	25	17	13	9

Chapter 4

RESULTS AND DISCUSSION

4.1 Results

4.1.1 Line-of-Sight Velocity Distributions: v, σ, h_3, h_4

Figures 4.1 - 4.4 show the intensity μ_I, velocity v, velocity dispersion σ, skewness h_3, and kurtosis h_4 as a function of distance from the center of the galaxy for each PA and offset. A S/N threshold of 10 was used for v and σ and a S/N of 13 for h_3 and h_4. For μ_I, the original and inverted profiles are shown as squares and triangles. For the kinematic profiles, triangles show the averaged (folded) values, while squares show the value of the one reliable side only when there are deviant points.

4.1.2 TW

Figures 4.9 - 4.12 show the results of the TW method. A plot of $< v >$ versus $< X >$ is shown for each PA. The three sets of points correspond to PAs of $0''$, $+11''$, and $-11''$. For a PA of 319°, only two points are available.

Table 4.1 summarizes the derived slopes for all PAs, assuming that the PA is along the line-of-nodes. To determine the values in Table 4.1, $< v >$ and $< X >$ measurements for each PA were fit using a linear least-square fitting routine in GNUPLOT. The resulting slope is then equal to $\Omega_p \sin(i)$ (in units of $\mathrm{km\,s^{-1}\,arcsec^{-1}}$), while the y-intercept (in $\mathrm{km\,s^{-1}}$) should be close to the galaxy's systemic velocity. Adopting a distance of 43.9 Mpc to NGC 5266, the third column in Table 4.1 gives the slope in units of $\mathrm{km\,s^{-1}\,kpc^{-1}}$.

4.2 Discussion

4.2.1 Surface Brightness Profiles

The surface brightness plots along each slit help to show asymmetries in the light profile. A few of the surface brightness plots are fairly symmetric, such as for a PA of 259°, offset=0″ (Figure 4.1), and for a PA of 274°, offset=± 11″ (Figure 4.2), but the rest show some evidence of asymmetry. The most likely explanation for this is NGC 5266's minor-axis dust lane. No matter the PA and offset used, some part of the dust lane will interfere. The dust causes light from the galaxy to be obscured, explaining the dips in the profiles. The error bars for v, σ, h_3, and h_4 do not appear affected by these asymmetries, but the dips may create a problem for the TW method (see 4.2.4).

4.2.2 Line-of-Sight Velocity Distributions: v, σ, h_3, h_4

The plots of the velocity and velocity dispersion contain the most accurate of the four measurements. For the most part, the velocity curves are well-behaved, flattening out at distances far from the center of the galaxy. The antisymmetry (i.e. change in sign) about the center indicates net rotation about the minor-axis of NGC 5266. The steep rise in the center of the rotation curve signifies fast rotation and

Table 4.1. Measurements of $\Omega_p \sin(i)$.

PA (degrees)	Slope ($\mathrm{km\,s^{-1}\,arcsec^{-1}}$)	Slope ($\mathrm{km\,s^{-1}\,kpc^{-1}}$)	Y-Intercept ($\mathrm{km\,s^{-1}}$
259	12 ± 2	56 ± 9	3065 ± 12
274	-15 ± 3	-70 ± 14	3082 ± 9
304	-22 ± 4	-103 ± 19	3055 ± 11
319	17 ± 3	80 ± 14	3042 ± 14

may indicate the presence of global rotational support (Binney & Merrifield 1998). Plots of v/σ may help to strengthen this idea (see Figures 4.5 – 4.8). The fact that many rotation curves show a double-hump also hints at a central stellar disk (Chung & Bureau 2004; Bureau & Athanassoula 2005).

Comparison with previous results for NGC 5266 shows that our velocity curves reach a lower maximum than those quoted elsewhere. While our data reach a maximum velocity of about $167\,\mathrm{km\,s^{-1}}$ at both a PA of 274° and 304°, Varnas et al. (1987) found a maximum stellar velocity of $212 \pm 7\,\mathrm{km\,s^{-1}}$ about the minor-axis of NGC 5266 (PA=287°). Extrapolating our data may help to show that our values fall within the error bars of Varnas et al. (1987) result.

In the case of the velocity dispersion profiles, each is symmetric about the center of the galaxy. In addition, each contains a dip in the center, with a less well-defined behavior farther out. Those dips can probably be explained by the dynamics in the galaxy's central region. An ionized gas disk is known to be present in the inner region of NGC 5266 (Varnas et al. 1987) and, although along the minor-axis, it could be at the origin of the velocity disperion dips if there is associated star formation. Indeed, stars born out of dynamically cold gas (i.e. a disk) will cause a dip at the center of the velocity dispersion profiles since their velocity dispersion is lower than that of the old stellar population (Wozniak et al. 2003). Cold gas naturally accumulates at the center of galaxies, due to dissipation and efficient cooling. In NGC 5266, this cold gas probably originated from merger activity. This is supported by the presence of the dust lane and warped gas disk, which are thought to have arisen from the merger of two spiral galaxies 1.2 Gyr ago (Morganti et al. 1997).

Again, comparing our results with those of Varnas et al. (1987), we find a stellar velocity dispersion of about $210\,\mathrm{km\,s^{-1}}$ at the center, which decreases to a value of about $156\,\mathrm{km\,s^{-1}}$ at a radius of R=20″. Varnas et al. (1987) also find $210 \pm 6\,\mathrm{km\,s^{-1}}$ at the center, but arrive at a minimum of $100 \pm 6\,\mathrm{km\,s^{-1}}$ for R=20″.

Plots of v/σ as a function of position are shown in Figures 4.5 – 4.8. In these plots, where $v/\sigma \approx 0$, the galaxy is supported by dispersion motions while $v/\sigma \approx 1$ signifies the galaxy is rotatationally-supported. Points where v/σ are greater that 1 are due to large error bars far from the galaxy's center. For the most part, v/σ is symmetric about the galaxy. The rise of v/σ is roughly linear with position from the galaxy's center for most of the PA's and offsets. These plots suggest that at the very center, NGC 5266 is dispersion-supported while farther out, the galaxy is mostly rotationally-supported.

For the h_3 and h_4 profiles, although the S/N thresholds are higher, the trends are not as clear as for v and σ. But in spite of this, our work represents the most detailed measurements of h_3 and h_4 for NGC 5266 to date. We see a clear anti-correlation of v and h_3 at the center. It is thus possible that the LOSVD contains two components there: a non-rotating broad distribution and a rapidly rotating narrow distribution (Binney & Merrifield 1998). This again supports the fast rotation of NGC 5266 and supports the presence of a rotationally-supported stellar disk at the galaxy's center. The fact that h_3 often correlates with v at large radius may suggest triaxiality of the main body (Bureau & Athanassoula 2005). Varnas et al. (1987) also suggest that the true shape of the stellar component is probably triaxial, or nearly oblate. This is

also consistent with the results of Morganti et al. (1997), who argue that NGC 5266 is the result of the merger of two gas-rich spirals 1.2 Gyr ago.

The kurtosis h_4 is mostly non-zero for NGC 5266 and varies in sign from plot to plot. In general, ellipticals tend to have positive values of h_4 within their effective radius, and zero or negative values past this radius (Binney & Merrifield 1998). Yet NGC 5266 does not show such a clear trend. However, the large error bars on these points prevent a robust interpretation.

For future work, interpolating between the multiple slit data would give a fuller description of the galaxy's kinematics, simulating a full kinematic field (as yielded by, e.g., integral field spectroscopy).

4.2.3 Errors

While the data in Figures 4.1 – 4.4 are highly reliable, the error bars are somewhat less accurate, as they were determined through a "folding" of the data. While this makes sense for the values of at an offset of 0″, it is wrong for any other offset. Indeed, data with non-zero offset are simply not expected to be symmetric with respect to the center (i.e., with respect to the maximum of the light profile) given the geometry of the system. Our procedure has thus caused the errors in the offset kinematic profiles to be overestimated, not because the measurements are bad, but rather because the profiles are not intrinsically symmetric. An independent method to derive the error bars (i.e. a Monte-Carlo simulation) would be more appropriate.

4.2.4 TW Results

From Table 4.1, it appears that the pattern speed values for from different PAs are not consistent with each other. Nevertheless, all lie within the values for found for barred disk systems using the TW method (Aguerri et al. 2003). While the slopes calculated at PAs of 274° and 304° or 259° and 319° are somewhat consistent with one another, the two pairs are not consistent.

At this time, the potential problems mentioned in Section 1.3 should be reexamined. First, the line-of-nodes in the system was determined using the location of the minor-axis dust lane. While no test was done to validate this (Debattista 2003), we are confident that the system geometry and rapid rotation are enough to roughly determine the line-of-nodes. As can be seen in the kinematic plots, the minor-axis dust lane also influences the results somewhat. It is unknown how this affects the TW results. Finally, the effects of vertical stellar streaming are poorly understood. We have no way of knowing if and how such stellar streaming has influenced these results, and its effects should be investigated further before more applications of the TW method to elliptical systems are done.

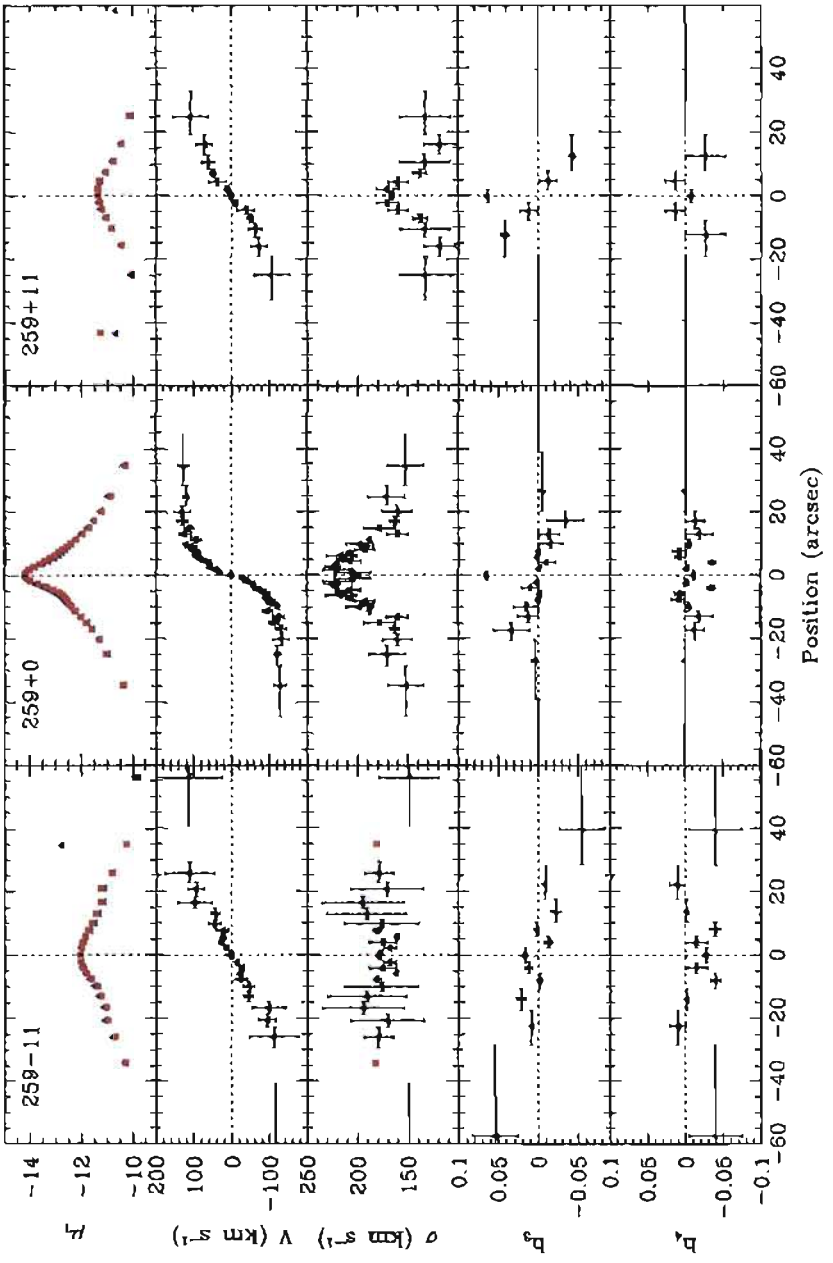

Fig. 4.1.— Plots of μ_I, v, σ, h_3, and h_4 as a function of position along the slit for NGC 5266, at a PA of 259° for offsets 0, -11, and +11 arcsec.

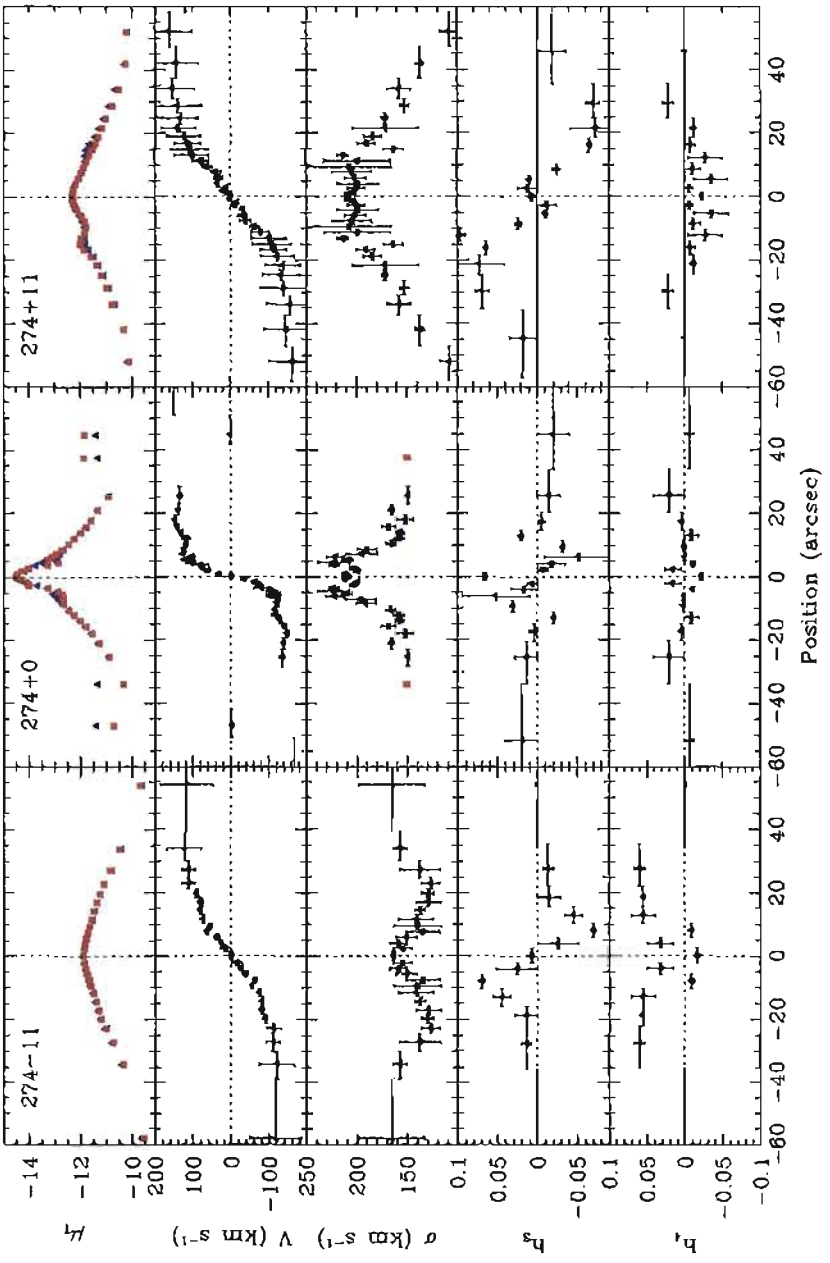

Fig. 4.2.— Plots of μ_I, v, σ, h_3, and h_4 as a function of position along the slit for NGC 5266, at a PA of 274° for offsets 0, -11, and +11 arcsec.

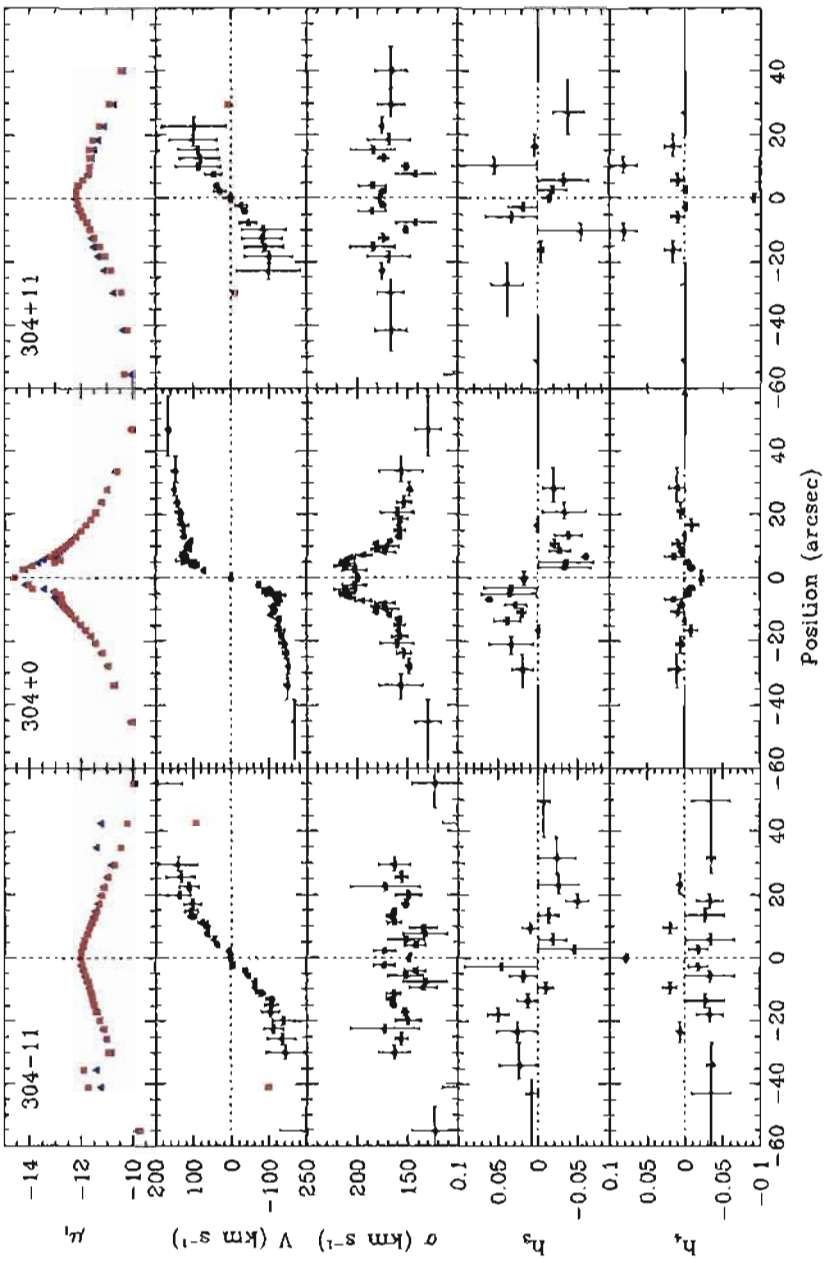

Fig. 4.3.— Plots of μ_I, v, σ, h_3, and h_4 as a function of position along the slit for NGC 5266, at a PA of 304° for offsets 0, -11, and +11 arcsec.

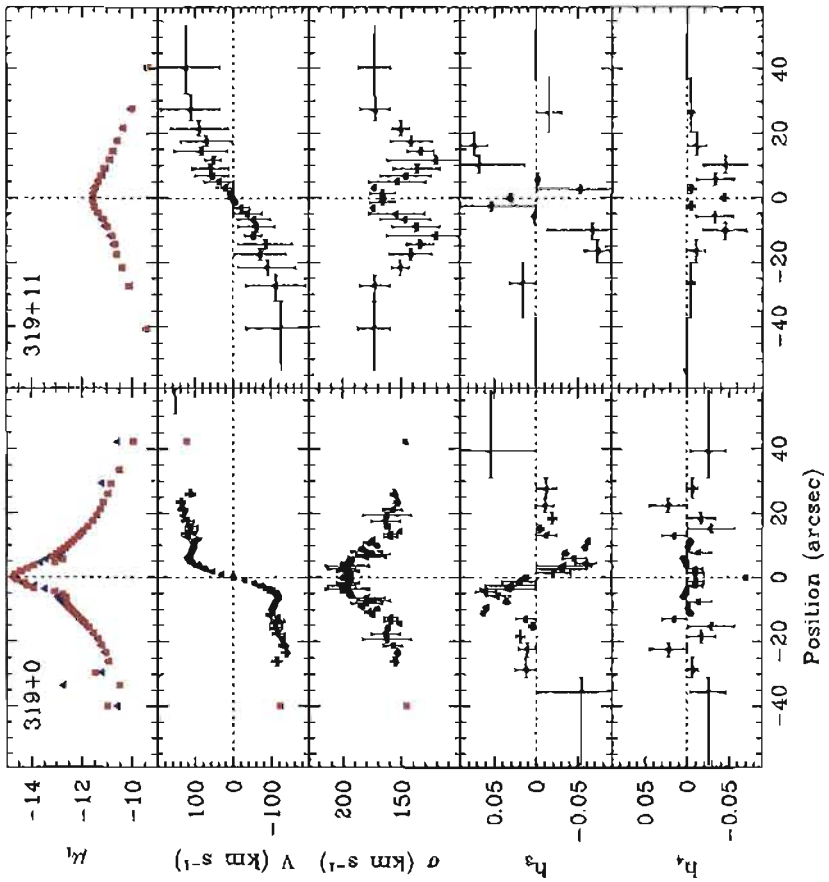

Fig. 4.4.— Plots of μ_I, v, σ, h_3, and h_4 as a function of position along the slit for NGC 5266, at a PA of 319° for offsets 0 and +11 arcsec.

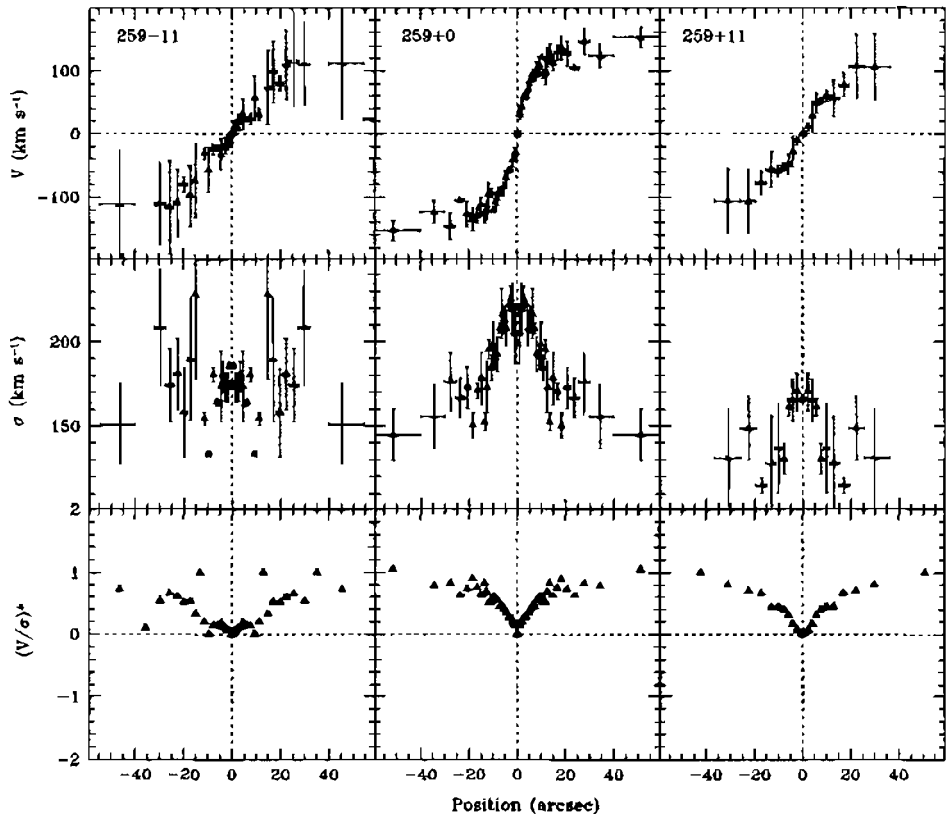

Fig. 4.5.— Plots of v, σ, and v/σ as a function of position along the slit for NGC 5266, at a PA of 259° for offsets 0, -11, and +11 arcsec.

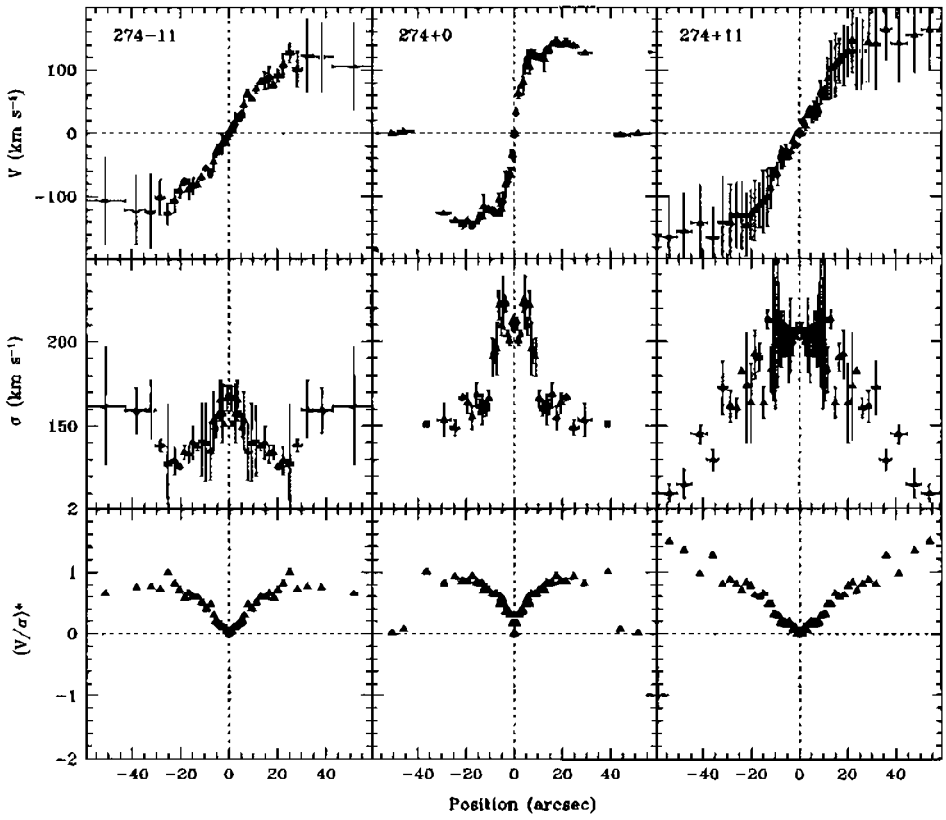

Fig. 4.6.— Plots of v, σ, and v/σ as a function of position along the slit for NGC 5266, at a PA of 274° for offsets 0, -11, and +11 arcsec.

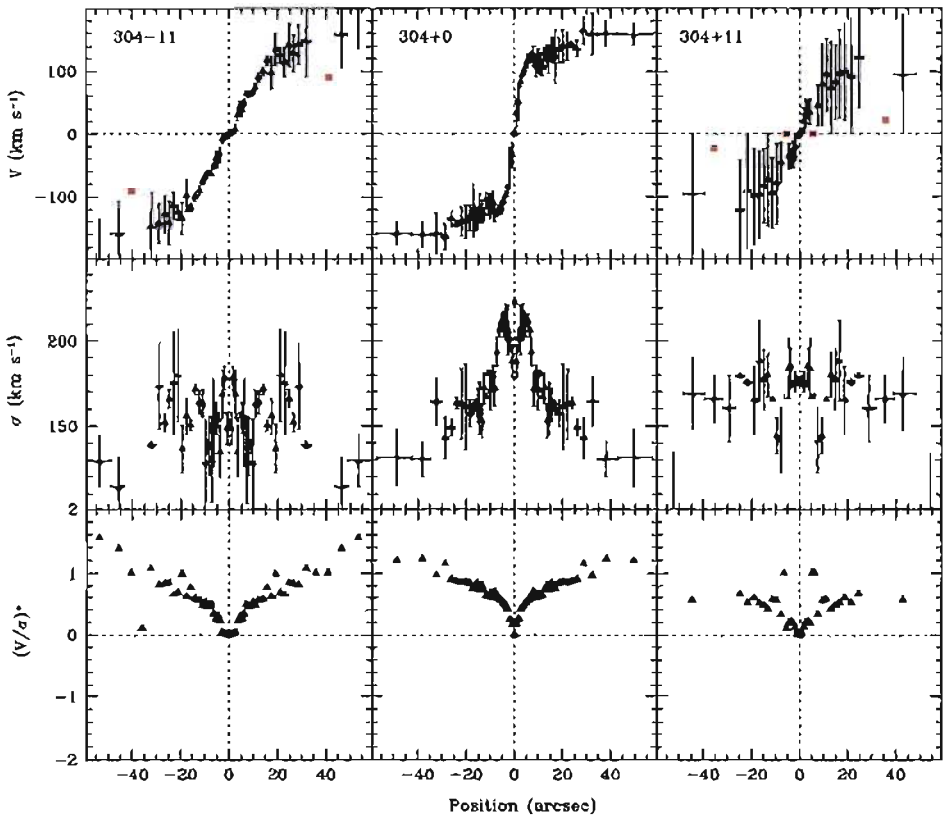

Fig. 4.7.— Plots of v, σ, and v/σ as a function of position along the slit for NGC 5266, at a PA of 304° for offsets 0, -11, and +11 arcsec.

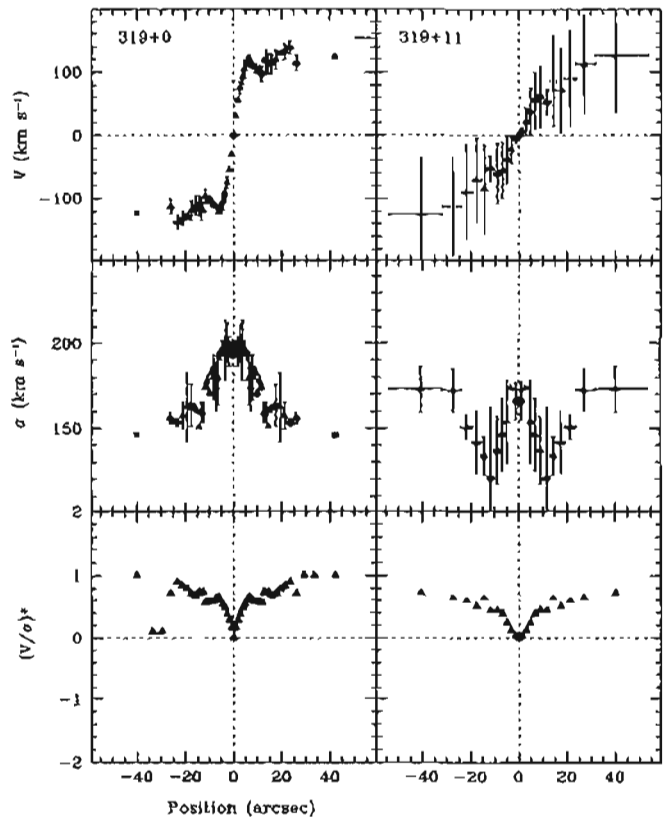

Fig. 4.8.— Plots of v, σ, and v/σ as a function of position along the slit for NGC 5266, at a PA of 319° for offsets 0 and +11 arcsec.

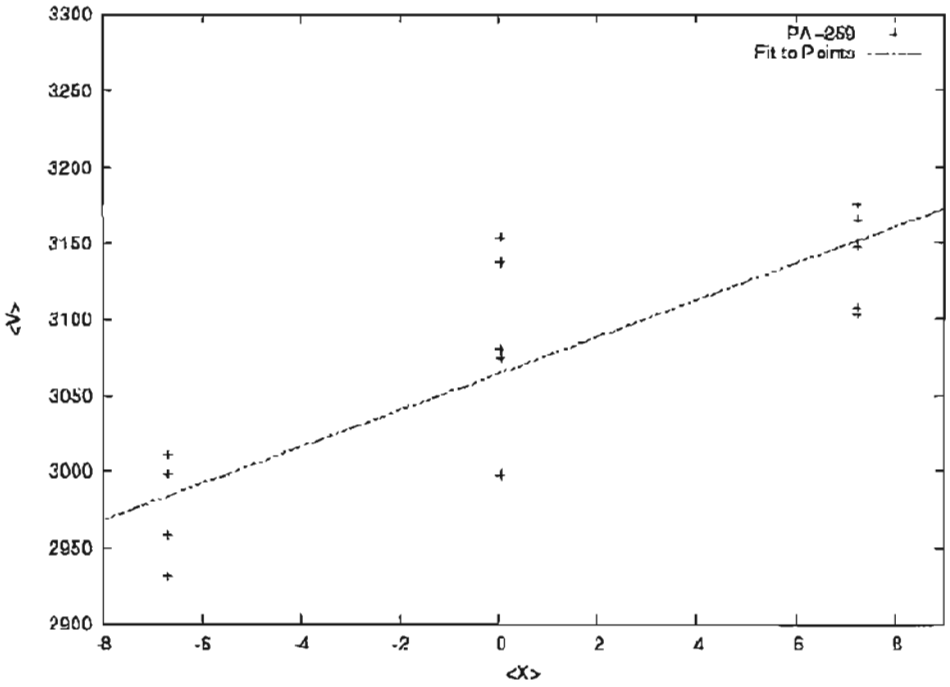

Fig. 4.9.— Pattern speed measurement of NGC 5266 for a PA of 259° using various template stars.

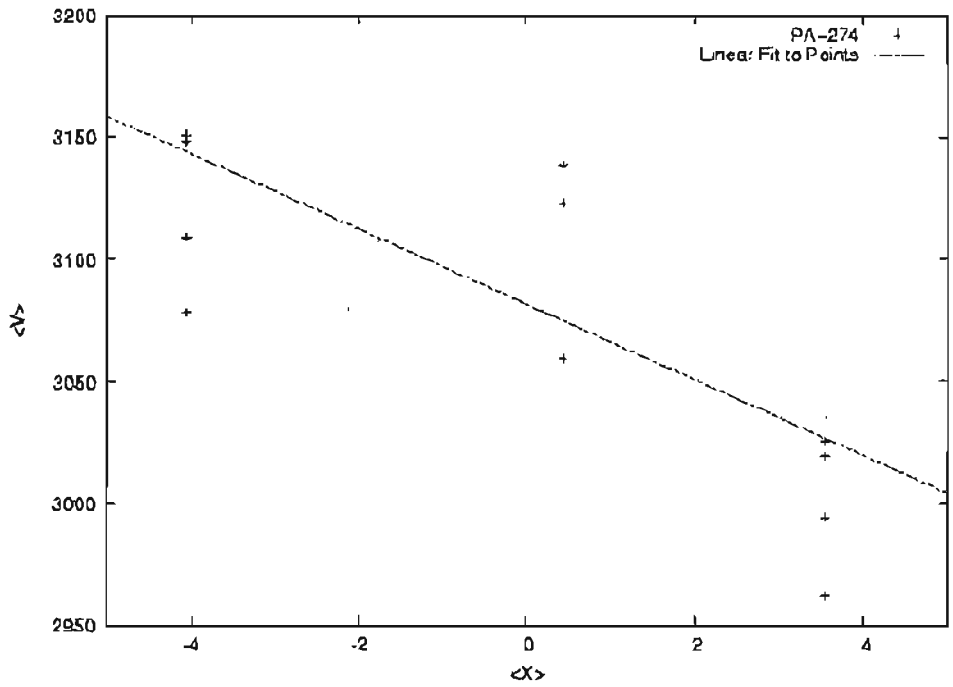

Fig. 4.10.— Pattern speed measurement of NGC 5266 for a PA of 274° using various template stars.

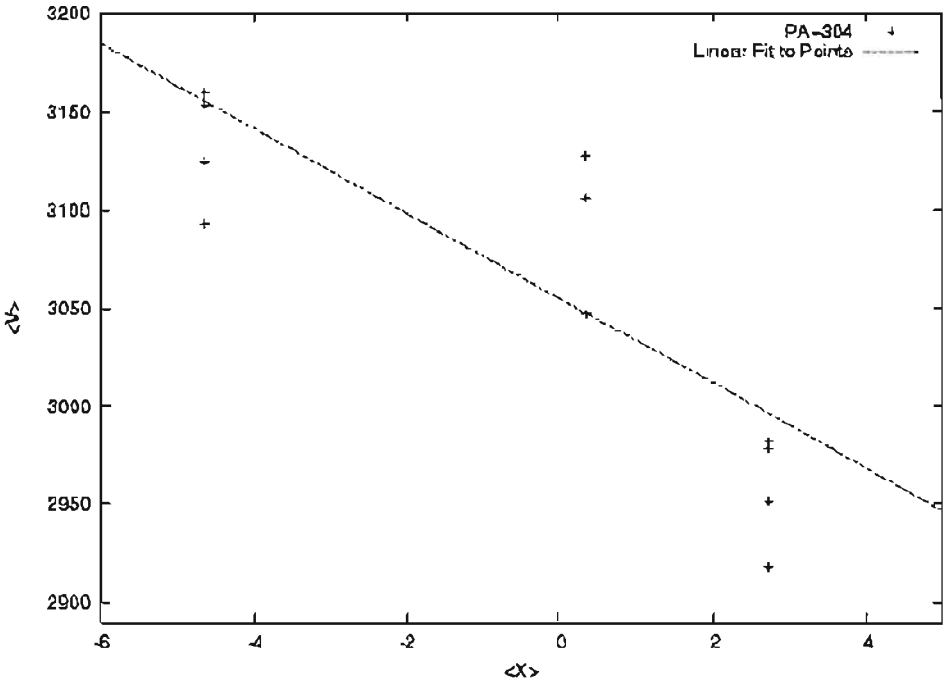

Fig. 4.11.— Pattern speed measurement of NGC 5266 for a PA of 304° using various template stars.

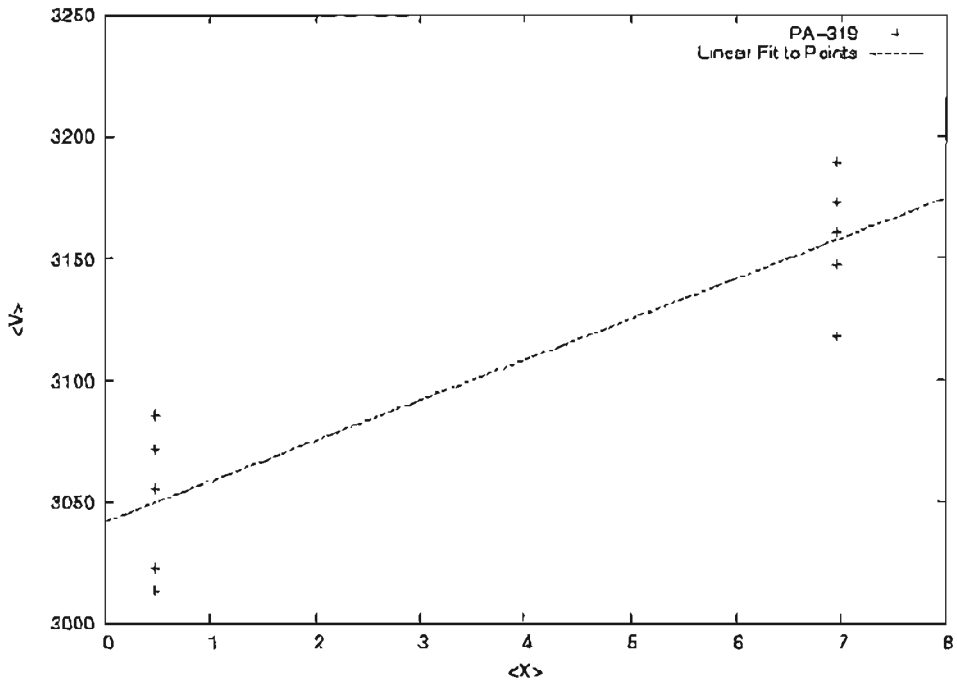

Fig. 4.12.— Pattern speed measurement of NGC 5266 for a PA of 319° using various template stars

Chapter 5

CONCLUSIONS

Using the long slit spectra of NGC 5266 along four PA's, each with different offsets, we have successfully derived the stellar kinematics (v, σ, h_3, and h_4) across much of the optical extent of the galaxy. We find a maximum velocity of about $167\,\mathrm{km\,s^{-1}}$ at both a PA of 274° and 304°. This is compared with a maximum stellar velocity of $212 \pm 7\,\mathrm{km\,s^{-1}}$ about the minor-axis of NGC 5266 from Varnas et al. (1987). We also find a stellar velocity dispersion of about $210\,\mathrm{km\,s^{-1}}$ at the center, which decreases to a value of about $156\,\mathrm{km\,s^{-1}}$ at a radius of R=20″. Varnas et al. (1987) also find $210 \pm 6\,\mathrm{km\,s^{-1}}$ at the center, but find a minimum of $100 \pm 6\,\mathrm{km\,s^{-1}}$ for R=20″. From the central anti-correlation of v and h_3, we find that NGC 5266 contains a non-rotating broad distribution and a rapidly rotating narrow distribution. The possible correlation at large radii suggests triaxiality of the main body. From these conclusions, we are confident that these results are accurate and reflect the true nature of the galaxy's internal kinematics. These results are consistent with those of Morganti et al. (1997), who suggest that NGC 5266 may have formed from the merger of two spiral galaxies.

The initial goal of this project was to test the TW method to measure the figure rotation of an elliptical galaxy with a minor-axis dust lane. We obtained values for the pattern speed, $\Omega_p \sin i$, between -22 and 17 km/s/arcsec, but these did not vary with position angle in a way that is consistent with figure rotation. Future applications of this method using integral field spectrographs will improve the kinematic information and bypass the necessity to know a priori the location of the line-of-nodes. Notwithstanding the issue of vertical streaming, this may allow measurements of the pattern speed of elliptical systems such as NGC 5266.

Chapter 6

APPENDIX

6.1 DETAILS OF TW CALCULATION

The following sets of tables list the values for $\Omega_p \sin i$ obtained from two different methods. Table 6.1 summarizes the notation used for columns labeled "template stars". In Tables 6.2 - 6.5, the values of $< V >$ and $< X >$ are determined from the data and $\Omega_p \sin i$ is calculated by directly dividing $< V >$ by $< X >$. A more accurate method for determining $\Omega_p \sin i$ should include the fitting of a linear function to the data. Table 6.6 includes the results using a linear, least-squares fitting method. This calculation uses a fitting routine in GNUPLOT. A second calculation was done using the IDL 'LINFIT' algorithm. The resulting parameters from 'LINFIT' are close to the values given by GNUPLOT and were not included here for this reason. The results from the linear, least-squares fit method are much more reliable than a direct calculation of the slope. The errors can also be determined from a fit to the three data points. Therefore, the slopes calculated using the second method were adopted for determining the best values for $\Omega_p \sin i$, listed in Table 4.1.

Table 6.1. Summary of Template Star Notation. Note that the April data consists of data taken at $274° + 11''$, $274° - 11''$, $304° + 11''$, and $304° - 11''$, while the May data cover the rest of the PAs and offsets

Temp. Star Number	Temp. Star Name	Type	Date of Observation
1	CPD-432527	K1III	7-Apr-1997
2	CPD-432527	K1III	8-Apr-1997
3	HD 176047	K1III	7-Apr-1997
4	HD 176047	K1III	8-Apr-1997
1	CPD-432527	K1III	10-May-1997
2	HD 176047	K1III	12-May-1997
3	HD 176047	K1III	13-May-1997
4	LTT 7379	G0	11-May-1997
5	LTT 7379	G0	13-May-1997

Table 6.2. $< X >$, $< V >$, and $\Omega_p \sin i$ for a PA of 259° and offsets $0''$, $+11''$, and $-11''$

PA+Offset	Temp. Star Number	$< X >$(arcsec)	$< V >(\mathrm{km\,s^{-1}})$	$< V > / < X > (\mathrm{km\,s^{-1}\,arcsec^{-1}})$
259+00	**1**	0.034	3075.156	90511.739
259+00	**2**	0.034	3137.282	92340.320
259+00	**3**	0.034	3153.713	92823.928
259+00	**4**	0.034	2997.956	88239.503
259+00	**5**	0.034	3081.068	90685.758
259+11	**1**	-6.697	2931.087	-437.664
259+11	**2**	-6.697	2998.479	-447.727
259+11	**3**	-6.697	3011.164	-449.621
259+11	4	-6.697	2958.530	-441.762
259+11	5	-6.697	2958.877	-441.814
259-11	**1**	7.237	3102.791	428.763
259-11	**2**	7.237	3165.790	437.469
259-11	**3**	7.237	3175.490	438.809
259-11	**4**	7.237	3147.626	434.959
259-11	5	7.237	3107.378	429.397

Table 6.3. $< X >$, $< V >$, and $\Omega_p \sin i$ for a PA of 274° and offsets 0″, +11″, and −11″

PA+Offset	Temp. Star Number	$< X >$(arcsec)	$< V >$(km s^{-1})	$< V > / < X >$(km s^{-1} arcsec^{-1})
274+00	1	0.432	3059.413	7088.348
274+00	2	0.432	3123.235	7236.216
274+00	3	0.432	3138.956	7272.641
274+00	4	0.432	3088.380	7155.460
274+11	1	-4.064	3078.182	-757.338
274+11	2	-4.064	3109.313	-764.997
274+11	3	-4.064	3151.040	-775.264
274+11	4	-4.064	3148.760	-774.703
274-11	1	3.537	2962.112	837.482
274-11	2	3.537	2994.313	846.586
274-11	3	3.537	3019.336	853.661
274-11	4	3.537	3025.402	855.376

Table 6.4. $< X >$, $< V >$, and $\Omega_p \sin i$ for a PA of 304° and offsets 0″, +11″, and −11″

PA+Offset	Temp. Star Number	$< X >$(arcsec)	$< V >$(km s^{-1})	$< V > / < X >$(km s^{-1} arcsec^{-1})
304+00	1	0.343	3047.074	8884.841
304+00	2	0.343	3106.444	9057.958
304+00	3	0.343	3127.686	9119.894
304+00	4	0.343	3068.287	8946.697
304+11	1	2.724	2918.251	1071.206
304+11	2	2.724	2950.704	1083.118
304+11	3	2.724	2978.071	1093.164
304+11	4	2.724	2981.292	1094.346
304-11	1	-4.650	3092.922	-665.144
304-11	2	-4.650	3125.166	-672.078
304-11	3	-4.650	3153.423	-678.155
304-11	4	-4.650	3160.119	-679.595

Table 6.5. $< X >$, $< V >$, and $\Omega_p \sin i$ for a PA of 319° and offsets 0″ and +11″

PA+Offset	Temp. Star Number	$< X >$(arcsec)	$< V >(\mathrm{km\,s^{-1}})$	$< V >/< X >(\mathrm{km\,s^{-1}\,arcsec^{-1}})$
319+00	**1**	0.479	3022.935	6315.948
319+00	**2**	0.479	3055.462	6383.907
319+00	**3**	0.479	3085.944	6447.595
319+00	4	0.479	3071.650	6417.731
319+11	**1**	6.958	3118.203	448.148
319+11	**2**	6.958	3173.154	456.046
319+11	**3**	6.958	3189.505	458.396
319+11	4	6.958	3147.282	452.328

Table 6.6. Linear Fit Values $\Omega_p \sin i$ and V_{sys} using the values for $< X >$ and $< V >$ in Tables 6.2 - 6.5

PA	Temp. Star Number	slope $(\mathrm{km\,s^{-1}\,arcsec^{-1}})$	y-intercept $(\mathrm{km\,s^{-1}})$
259	111	12.224 ± 5.063	3034.01 ± 28.82
259	**222**	11.9138 ± 4.803	3098.24 ± 27.34
259	**333**	11.6912 ± 5.233	3111.22 ± 29.79
259	**444**	13.6552 ± 4.301	3032.09 ± 24.49
259	555	10.576 ± 4.18	3047.09 ± 23.79
274	111	-14.4779 ± 7.494	3032.77 ± 23.39
274	**122**	-14.8412 ± 2.722	3053.87 ± 8.495
274	**233**	-16.5313 ± 7.526	3097.34 ± 23.49
274	**244**	-15.4756 ± 7.127	3098.64 ± 22.24
274	**333**	-16.2818 ± 9.888	3102.59 ± 30.86
274	**344**	-15.2261 ± 9.489	3103.89 ± 29.61
304	111	-21.4609 ± 10.88	3008.09 ± 33.94
304	122	-22.4278 ± 6.017	3029.15 ± 18.76
304	**233**	-21.5739 ± 10.78	3067.93 ± 33.62
304	**244**	-22.1786 ± 10.13	3070.92 ± 31.59
304	333	-20.9211 ± 13.98	3075.36 ± 43.58
304	344	-21.5258 ± 13.32	3078.34 ± 41.54
319	**11**	14.7033	3015.9
319	**22**	18.1641	3046.77
319	**33**	15.9832	3078.29
319	**44**	11.6728	3066.06
319	**55**	22.7327	3002.53

References

Aguerri, J. A. L., Debattista, V. P., Corsini, E. M., 2003, Mon. Not. R. Astron. Soc., 338, 465

Bacon, R., Copin, Y., Monnet, G., Miller, B. W., Allington-Smith, J. R., Bureau, M., Carollo, C. M., Davies, R. L., Emsellem, E., Kuntschner, H., Reynier, F. P., Verolme, E. K., de Zeeuw, P. T., 2001, Mon. Not. R. Astron. Soc., 326, 30

Bailin, J., Steinmetz, M., 2004, Astrophys. J., 616, 27

Bender, R., 1990, Astron. Astrophys., 229, 441

Bertola, F., Galletta, G., Zeilinger, W. W., 1985, Astrophys. J., 292, L51

Binney, J., 1982, Ann. Rev. Astron. Astrophys., 20, 399

Binney, J., Merrifield, M. R., 1998, Galactic Astronomy (Princeton: Princeton Univ. Press)

Bureau, M., Athanassoula, E., 2005, Astrophys. J., 626, 159

Caldwell, N., 1984, Astrophys. J., 278, 96

Chung, A., Bureau, M., 2004, Astrophys. J., 127, 3192

de Vaucouleurs, G. 1948, Ann. Astrophys., 11, 247

de Zeeuw, P. T., Franx, M., 1991, Ann. Rev. Astron. Astrophys., 29, 239

de Zeeuw, P.T., et al., 2002, Mon. Not. R. Astron. Soc., 329, 513

Debattista, V. P., 2003, Mon. Not. R. Astron. Soc., 342, 1194

Faber, S. M., 1979, Ann. Rev. Astron. Astrophys., 17, 135

Faber, S. M., Jackson, R.E., 1976, Astrophys. J., 204, 668

Franx, M., Illingworth, G. D., 1988, Astrophys. J., 327, L55

Gerhard, O. E., 1993, Mon. Not. R. Astron. Soc., 265, 213

Kuijken, K., Merrifield, M. R., 1993, Mon. Not. R. Astron. Soc., 264, 712

Merrifield, M. R., Kuijken, K., 1995, Mon. Not. R. Astron. Soc., 274, 933

Merritt, D., 1999, Proceedings of the Astronomical Society of the Pacific, 111, 129

Morganti, R., Sadler, E. M., Oosterloo, T., Pizzella, A., Bertola, F., 1997, Astrophys. J., 113, 937

Poveda, A., 1958, Bol. Obs. Tonantz. Tacub. 17, 3

Rodgers, A. W., Conroy, P., Bloxham, G., 1988, Astronomical Society of the Pacific, 100, 626

Sandage, A., Bedke, J., 1994, The Carnegie Atlas of Galaxies, Volume I (Washington, DC: Carnegie Institution)

Sargent, W. L. W., Schechter, P. L., Boksenberg, A., Shortridge, K., 1977, Astrophy. J., 212, 326

Simkin, S. M., 1974, Astron. Astrophys., 31, 129

Sparke, L. S., Gallagher, J.S., 2000, Galaxies in the Universe: An Introduction (New York, NY: Cambridge University Press)

Tody, D., 1986, "The IRAF Data Reduction and Analysis System" in Proc. SPIE Instrumentation in Astronomy VI, ed. D.L. Crawford, 627, 733

Tremaine, S., Weinberg, M. D., 1984, Astrophys. J., 282, L5

van Albada, T. S., Kotanyi, C. G., Schwarzschild, M., 1982, Mon. Not. R. Astron. Soc., 198, 303

van der Marel, R. P., Franx, M., 1993, Astrophys. J., 407, 525

Varnas, S. R., Bertola, F., Galletta, G., 1987, Astrophys. J., 313, 69

Wozniak, H., Combes, F., Emsellem, E., Friedli, D., 2003, A & A, 409, 467